



Theory of Figures to the Seventh Order and the Interiors of Jupiter and Saturn

N. Nettelmann^{1,2} , N. Movshovitz¹ , D. Ni³ , J. J. Fortney¹ , E. Galanti⁴ , Y. Kaspi⁴ , R. Helled⁵ ,
C. R. Mankovich⁶ , and S. Bolton⁷

¹ Department of Astronomy and Astrophysics, University of California, Santa Cruz, CA 95064, USA⁸

² Institute of Planetary Research, German Aerospace Center, D-12489 Berlin, Germany

³ State Key Laboratory of Lunar and Planetary Sciences, Macau University of Science and Technology, Macao, People's Republic of China

⁴ Department of Earth and Planetary Sciences, Weizmann Institute of Science, Rehovot, 7610001, Israel

⁵ Center for Theoretical Astrophysics and Cosmology, Institute for Computational Science, University of Zurich, CH-8057 Zürich, Switzerland

⁶ Division of Geological and Planetary Sciences, Mailcode 150-21, Caltech, Pasadena, CA 91125, USA

⁷ Southwest Research Institute, San Antonio, TX 78238, USA

Received 2021 June 21; revised 2021 October 21; accepted 2021 October 27; published 2021 December 15

Abstract

Interior modeling of Jupiter and Saturn has advanced to a state where thousands of models are generated that cover the uncertainty space of many parameters. This approach demands a fast method of computing their gravity field and shape. Moreover, the Cassini mission at Saturn and the ongoing Juno mission delivered gravitational harmonics up to J_{12} . Here we report the expansion of the theory of figures, which is a fast method for gravity field and shape computation, to the seventh order (ToF7), which allows for computation of up to J_{14} . We apply three different codes to compare the accuracy using polytropic models. We apply ToF7 to Jupiter and Saturn interior models in conjunction with CMS-19 H/He equation of state. For Jupiter, we find that J_6 is best matched by a transition from an He-depleted to He-enriched envelope at 2–2.5 Mbar. However, the atmospheric metallicity reaches $1 \times$ solar only if the adiabat is perturbed toward lower densities, or if the surface temperature is enhanced by ~ 14 K from the Galileo value. Our Saturn models imply a largely homogeneous-in-Z envelope at $1.5\text{--}4 \times$ solar atop a small core. Perturbing the adiabat yields metallicity profiles with extended, heavy-element-enriched deep interior (diffuse core) out to $0.4 R_{\text{Sat}}$, as for Jupiter. Classical models with compact, dilute, or no core are possible as long as the deep interior is enriched in heavy elements. Including a thermal wind fitted to the observed wind speeds, representative Jupiter and Saturn models are consistent with all observed J_n values.

Key words: Jupiter – Planetary interior – Saturn

Supporting material: machine-readable table

1. Introduction

Since the era of the Voyager 1 and 2 gravity field determinations and shape measurements of the outer planets, only two methods have extensively been employed to calculate the shape and gravity field from interior models to compare with the data. These methods are the theory of figures (ToF; Zharkov & Trubitsyn 1978) and the Concentric Maclaurin Spheroid (CMS) method (Hubbard 2012, 2013). ToF has served that purpose before the advent of accurate gravity data from Juno at Jupiter and from the Cassini Grand Finale Tour at Saturn. Beforehand, only the gravitational moments J_2 , J_4 , and J_6 were measured, and the smallest given uncertainty in Jupiter's J_6 of 10% was still rather large (Jacobson 2003).

The low-order gravitational harmonics are important observables, as they constrain the density profile about midway into the planetary interior. They are expansion coefficients of the external planetary gravity field evaluated at a reference radius in the equatorial plane, R_{eq} , which encompasses the planet's total mass. They are defined as integrals over density $\rho(r)$ in the

planet's interior,

$$J_n = -\frac{1}{M R_{\text{eq}}^n} \int d^3r \rho(\vec{r}) r^n P_n(\cos \vartheta), \quad (1)$$

where P_n are the Legendre polynomials and ϑ is colatitude. Thanks to the Juno and Cassini missions, the observational accuracy in the even harmonics J_{2n} has seen significant improvement (Iess et al. 2018, 2019; Durante et al. 2020). For both Jupiter and Saturn, the uncertainties in the low-order harmonics reduced to a level that can be considered exact from the perspective of adjusting internal density distributions to reproduce the data. However, significant spread in the deep interior density distributions is still possible (see Movshovitz et al. 2020 for Saturn), as the sensitivity of the J_{2n} toward the center fades with $(r/R_{\text{eq}})^{2n}$ (see Equation (1)). This spread is a residual uncertainty related to other causes such as the positioning of internal helium gradients due to uncertainty in the H–He phase diagram, the temperature profile in stably stratified regions, the H–He equations of state (EOSs), or the positioning of heavy-element gradients due to uncertainties in planet formation and evolution.

ToF to the fourth order (ToF4) has been deemed sufficiently accurate for computation of J_2 and J_4 usually used to constrain the density distribution (Nettelmann 2017). Higher-order moments beyond J_4 have been provided to a precision in J_6 to J_{10} of better than $(0.01\text{--}0.1) \times 10^{-6}$ for Jupiter (Durante et al. 2020) and $(0.1\text{--}1) \times 10^{-6}$ for Saturn (Iess et al. 2019), but as

⁸ Juno Participating Scientist.



Original content from this work may be used under the terms of the [Creative Commons Attribution 4.0 licence](https://creativecommons.org/licenses/by/4.0/). Any further distribution of this work must maintain attribution to the author(s) and the title of the work, journal citation and DOI.

the order increases, so does the influence by the zonal flows on the harmonics. At present, this is where the limitations of the ToF method become evident. ToF is an expansion method. An n th-order expansion (ToF n) allows us to compute up to J_{2n} and to an error of the order of q_{rot}^{n+1} , where $q_{\text{rot}} = \omega^2 R_{\text{eq}}^3 / \text{GM}$ is the ratio of centrifugal to gravitational force at the equatorial radius. The highest presented ToF order so far is 5 (Zharkov & Trubitsyn 1975). It has recently been applied to compute Saturn's J_2 – J_{10} values (Ni 2020); however, its accuracy has not been validated yet.

Although the CMS method is also an expansion method, it can conveniently be carried out to the order of 15–20 or higher (Hubbard 2013). Therefore, it enables high-accuracy computation of the high-order J_{2n} up to the order of the measurements (Wahl et al. 2017b; Militzer et al. 2019). The CMS method provides further advantages, such as its expansion to 3D to account for tidal shape and gravity field perturbations (Wahl et al. 2017a) and brevity in its formulation (Hubbard 2013). Its only drawback is that the CMS method goes along with high computational cost even in its accelerated version (Militzer et al. 2019). This is because the CMS method explicitly solves for the 2D planetary shape not only by taking the sum over radial spheroids but also by integrating over latitude. Even if making use of Gaussian quadrature, typically several tens of angular grid points are required. If the integrand were a polynomial, only $N_{\text{lat}} = n + 1$ grid points would be required to evaluate the integrals over P_{2n} , which for J_{12} ($n = 6$) amounts to only $N_{\text{lat}} = 7$, or even 4 points when accounting for hemispheric symmetry. However, the integrands are functions of the nonpolynomial shape itself. In practice, 48 grid points (Wahl et al. 2017a) are used. Obtaining the shape to sufficient accuracy at these grid points is the most time-consuming part of the CMS method. In contrast, ToF solves for the shape explicitly only in the equatorial plane, while the shape at higher latitudes is obtained by spherical harmonics expansion, and the required precision of the shape is only the one wanted for the J_{2n} . One may thus see a benefit in using ToF for computation of the high-order moments.

Here we introduce ToF7 tables, which allow one to calculate up to J_{14} . In Section 2, we give an overview of the ToF method, while for further details we refer to the Appendix. In Section 3, we assess the accuracy of the ToF method by comparing to the analytic $n = 1$ polytrope solution. In Section 4, we apply the new tables to Jupiter models, and in Section 5 we apply them to Saturn. In Section 6, we connect representative interior models to thermal wind models to predict the wind decay depth profiles. Observing notoriously low atmospheric metallicities of our Jupiter models, we discuss further influences in Section 7. Section 8 concludes the main body of the paper. In Appendix A.3 we introduce the ToF7 tables for public usage.

2. Theory of Figures

The ToF is described in Zharkov & Trubitsyn (1978), and the coefficients up to the third order are presented therein. Nettelmann (2017) followed their notation and calculated the fourth-order coefficients. We note that fifth-order coefficients were presented in Zharkov & Trubitsyn (1975) and adopted by Ni (2020) for application to Saturn. Building on the work of Nettelmann (2017), we here conduct the expansion of ToF to the seventh order, meaning that the even harmonics up to J_{14} can be calculated.

Both the ToF and CMS methods assume that surfaces of equal potential U exist on which density and pressure are constant. One

can show that this assumption holds for planets in hydrostatic equilibrium that rotate along cylinders, e.g., if their rotation rate can be expressed as $\vec{\omega} = \omega(s) \vec{e}_\omega$ with axis distance s . Rigid rotation and no rotation meet this condition. For rotation along cylinders, the odd harmonics J_{2n+1} disappear. However, the Juno measurements at Jupiter (Iess et al. 2018; Durante et al. 2020) and Cassini Grand Finale at Saturn (Iess et al. 2019) revealed that these planets' odd harmonics are nonzero. Instead, they are of the order of 0.1×10^6 , comparable to the values of J_{10} , J_{12} , and Saturn's uncertainty in J_6 . Based on the commonly used approach of using the thermal wind equation (TWE) to infer the density anomalies (Kaspi et al. 2010; Kaspi 2013), the depth of the wind-induced deviation from cylinder rotation has been inferred to be about 3000 km ($\sim 0.035 R_{\text{Jup}}$) in Jupiter (Kaspi et al. 2018) and 9000 km ($\sim 0.14 R_{\text{Sat}}$) in Saturn (Galanti et al. 2019). These results are consistent with the tangent-cylinder model of Dietrich et al. (2021), which goes beyond the TWE simplification by including not only the wind-induced density perturbation but also the associated gravitational perturbation, which has long been argued to be significant (Zhang et al. 2015). Taking into account also constraints from the observed secular variation of the magnetic field on deep flows (Moore et al. 2019) suggests a somewhat steeper decay function for the winds, with the zonal flow extending inward on cylinders almost barotropically to a depth of about 2000 km on Jupiter and 8000 km on Saturn, and then the winds decay abruptly within the next 1000 km (Galanti & Kaspi 2021). While the nonaxisymmetric gravity field is important for these width depth issues, here we have to neglect the asymmetries, as otherwise neither the ToF nor the CMS method could be applied.

In the absence of tides, the problem at hand is axisymmetric and thus 2D: r, ϑ . In ToF, the description is further reduced to 1D by introducing the mean radius coordinate l . Spheres of radius l are defined by the condition that they enclose the same volume as the equipotential surface $r_l(\vartheta)$,

$$\frac{4\pi}{3} l^3 = 2\pi \int_0^\pi \sin \vartheta d\vartheta \int_0^{r_l(\vartheta)} dr r'^2. \quad (2)$$

On the surface of the planet,

$$\frac{4\pi}{3} R_m^3 = 2\pi \int_0^\pi \sin \vartheta d\vartheta \int_0^{R(\vartheta)} dr r'^2,$$

with $R(\pi/2) = R_{\text{eq}}$. In ToF, the potential is thus constant on spheres. Both the total potential $U(l)$ and the axisymmetric 2D shape $r_l(\vartheta)$ are expanded into Legendre polynomials. One can write

$$U(l) = \frac{\text{GM}}{R_m} \left(\frac{l}{R_m} \right)^2 \sum_{k=0}^O A_{2k}(l) P_{2k}(\cos \vartheta), \quad (3)$$

while the shape of an equipotential surface, also called level surface, is given by

$$r_l(\vartheta) = l \left(1 + \sum_{k=0}^O s_{2k}(l) P_{2k}(\cos \vartheta) \right), \quad (4)$$

where the $s_{2k}(l)$ are the figure functions. The condition that $U(l)$ is constant on spheres of radius l implies that $A_{2k} = 0$ for $k > 0$. These expansions are carried out up to an order O . In the absence of tides, U is a superposition of only the gravitational potential V and the centrifugal potential Q so that $U = V + Q$ and $A_{2k} = A_{2k}^{(V)} + A_{2k}^{(Q)}$. By definition, the gravitational

harmonics J_{2n} can be obtained in the ToF as

$$J_{2i} = -(R_m/R_{\text{eq}})^{2i} S_{2i}(1), \quad (5)$$

where the integrals S_{2i} , not to be confused with the figure functions s_{2i} , are given by Equation (A7) in the Appendix. However, using Equation (A7) for the S_n and the ToF expansion coefficients to calculate the functions f_n on which the S_n depend (see Equations (A7) and (A9) in the Appendix) implies that only information on the equatorial radius $r(\pi/2)$ enters the computation of the J_{2n} , while information on the full shape $r(l, \theta)$ is reduced to the order of the expansion, that is, up to P_{14} . An alternative method is to calculate the integrals over latitude explicitly. In Section 3.3 we compare both methods. For details on how the ToF coefficients are computed and for an example of the machine-readable ASCII tables that contain their values for public usage, see Appendix A.3. Moreover, to facilitate the application of our ToF7 tables, we share computer routines for read-in of the tables and documentation at <https://doi.org/10.6084/m9.figshare.16822252>.

3. Validation against the $n = 1$ Polytrope

The $n = 1$ polytropic planet is specified by a number of conditions. First, the polytropic EOS $P = K \rho^2$. Furthermore, the gravity field of the rotating polytrope depends on the values of q_{rot} , equatorial radius R_{eq} , and planet mass M . The density profile $\rho(r)$ is not known in advance but is obtained from solution of the equation of hydrostatic equilibrium, $\nabla P / \rho = \nabla U$. In ToF, the radial coordinate r is transformed to the level surface l , and the equation of hydrostatic equilibrium reduces to $dP/dl = \rho dU(l)$. The internal m - l relation is obtained by integrating the equation of mass conservation, $m(l) = 4\pi \int_0^l dl \rho(l) l^2$. The latter is a source of numerical inaccuracy. We employ three different codes to compute the solution to the rotating polytrope. All polytropic models use $q_{\text{rot}} = 0.089195487$ and $\text{GM} = 126686536.1 \times 10^9 \text{ km}^3 \text{ s}^{-1}$ as in Wisdom & Hubbard (2016).

Before we compare the results of our application of three different codes and different orders of expansion of ToF to the analytic, Bessel-function-based method of Wisdom & Hubbard (2016) in Figure 1, we describe each of the three employed methods in Sections 3.1–3.3.

3.1. Polytrope with MOGROP

In the MOGROP code (Nettelmann 2017), the constant K is adjusted to fit the mass M . The mean radius R_m is adjusted to fit R_{eq} . The radial grid, for this application, is split into N grid points, out of which $N/2$ are equally distributed over 0 – $0.95 R_m$, and the other half equally over 0.95 – $1 R_m$. Such a choice was found to give a better match to the analytic solution than a split at $0.9 R_m$ or deeper. Indeed, with MOGROP, we find that the accuracy increases the farther out the separation is made, with a difference up to an order of magnitude compared to a flat distribution. The integrals in Equations (A7, A8) are converted into integrals over density by partial integration and solved by the simple trapezoidal rule. The integration of the equations of mass conservation, $dm/dl = 4\pi l^2 \rho(l)$, and hydrostatic equilibrium, $(1/\rho(l))dP/dl = dU/dl$, is performed by the Runge–Kutta fourth-order method. The J_{2n} are computed using Equation (5) and denoted by “4,7/Ne” and shown as green curves in Figure 1.

3.2. Polytrope with TOF-PLANET

The second code we use in our $n = 1$ polytrope comparison test case is an independent implementation of the ToF algorithm using the same coefficients but otherwise unrelated to the MOGROP code. The two codes are therefore expected to reproduce very similar solutions if given the same conditions. TOF-PLANET has previously been applied in a Bayesian study of Saturn’s possible interior (Movshovitz et al. 2020). Since for that purpose it was necessary to run tens of millions of density models to draw representative statistical samples, the code had to be optimized for speed and memory usage. An optional feature allows the shape functions to be explicitly calculated on a subset of level surfaces, while the shape of the rest can be spline interpolated in the radial direction. This “skip-n-spline” trick can provide a significant speed advantage when high-resolution density profiles are needed. We find that, even when a very high resolution of the density profile is required to accurately calculate integrals over density, there is no advantage in calculating the shape functions for more than a few hundred level surfaces. The speed advantage of this optimization applies mainly to high-resolution ToF7 calculations. For lower resolution, and for most ToF4 runs, the interpolation overhead ruins the effort. (ToF7 is much slower than ToF4 for a given N owing to the many more terms appearing in each of the shape function equations.)

To validate TOF-PLANET with both ToF4 and ToF7 coefficients, we use it to reproduce the $n = 1$ polytrope test of Wisdom & Hubbard (2016). To make a direct comparison in a consistent way, some care is needed. The mass and equatorial radius are taken as in Wisdom & Hubbard (2016) and remain fixed for the duration of the calculation. (The mass is taken from the reported GM and with $G = 6.6738480 \times 10^{-11} \text{ m}^3 \text{ kg}^{-1} \text{ s}^{-2}$.) However, in Wisdom & Hubbard (2016) the rotation state is given by the parameter q_{rot} , whereas the ToF algorithm needs the related parameter m_{rot} . The conversion needs the ratio R_{eq}/R_m , which is only available after the equilibrium shape is solved. To obtain a self-consistent solution, we fix the planet’s rotation frequency ω using the value $q_{\text{rot}} = 0.089195487$. We then proceed with a guess for R_{eq}/R_m and therefore m_{rot} , solve for the shape function and gravity field, integrate the hydrostatic equilibrium equation to solve for pressure everywhere, update the density everywhere to match the polytropic relation, renormalize the level radii grid to match the reference equatorial radius, renormalize the density to match the reference mass, recalculate m_{rot} for the updated $R_{\text{eq}}/R_{\text{mean}}$ ratio, and rerun all the steps until a self-consistent solution is found.

In this test, for both ToF7 and ToF4, we compute all integrals with the trapezoidal rule and constant grid spacing. With TOF-PLANET, we experimented and found that different integration schemes and grid spacing schemes did not reduce substantially the number of grid points required for a given precision. This should not discourage, however, future users of our ToF7 tables from optimizing their grids and integration schemes for their particular cases.

The resultant J_{2n} values appear in blue and are denoted by “4,7/Mo” in Figure 1.

3.3. Polytrope with CEPAM

As in previous work (Ni 2020), we apply the CEPAM code (Guillot & Morel 1995) to calculate the gravity field and shape using ToF5 (Zharkov & Trubitsyn 1975). Here we have expanded the code to address the case of the rotating $n = 1$ polytrope.

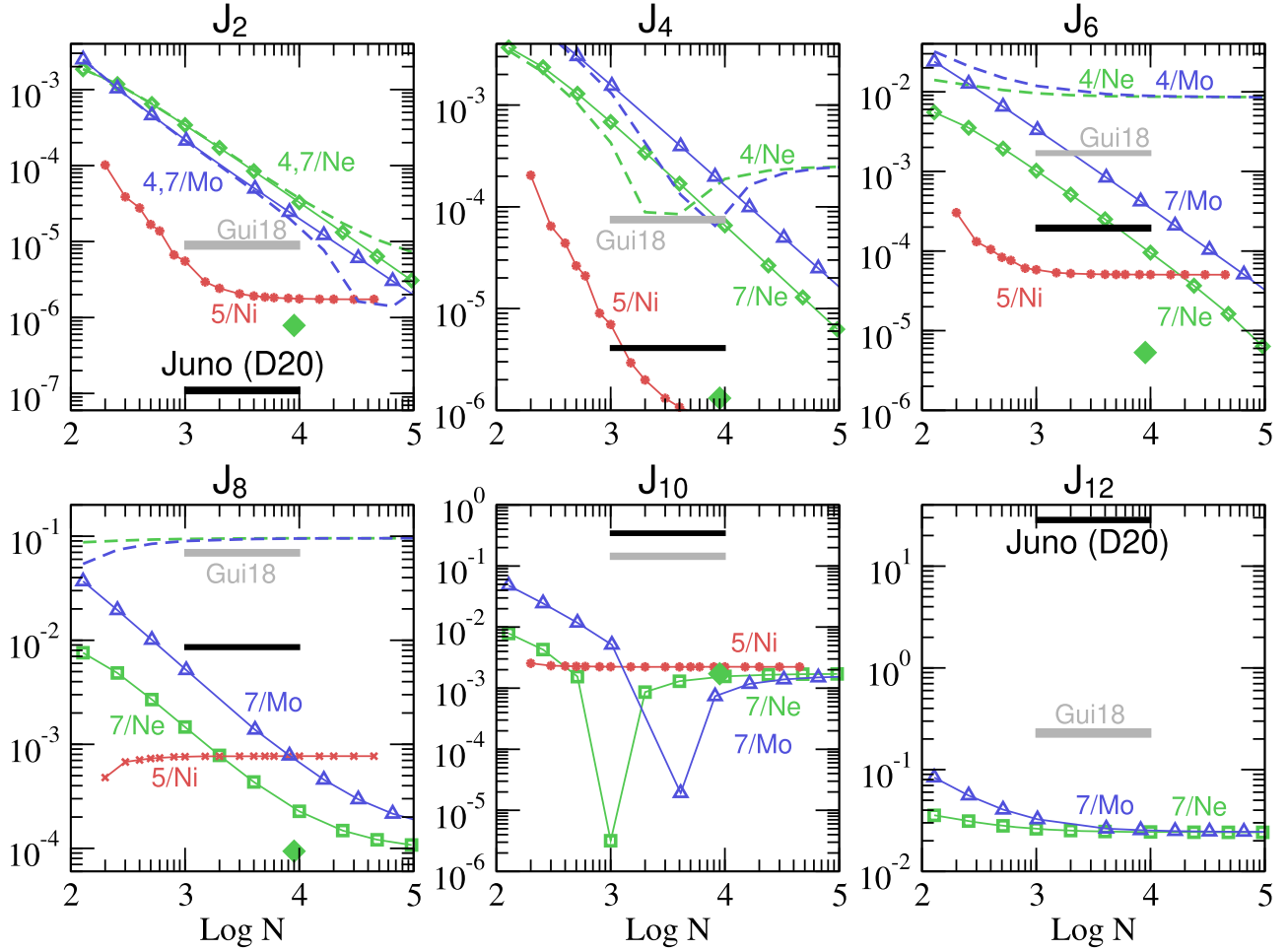


Figure 1. Relative differences $|\Delta J_n/J_n|$ between ToF solutions and the analytic Bessel-function-based solution (Wisdom & Hubbard 2016). Dashed lines (green and blue): ToF4; lines with open symbols (green and blue): ToF7; red lines with stars: ToF5 using CEPAM and labeled 5/Ni; green lines and labeled 4/Ne or 7/Ne: using MOGROP; blue lines and labeled 4/Mo or 7/Mo: using TOF-PLANET; gray bars labeled Gui18: CEPAM-WH16 from Guillot et al. (2018); black bars labeled Juno (Du20): obs. uncertainty (Durante et al. 2020). X-axis shows number N of radial grid points used in this work. Green diamonds placed at $N = 9000$ are for extrapolated J_{2n} values based on linear regression on the three computed values at $N = 1000, 2000$, and 4000 .

For the $n = 1$ polytropic EOS $P = K\rho^2$, the constant K is determined in terms of mass conservation, and the mean radius R_m is adjusted to reproduce the equatorial radius $R_{eq} = 71,492$ km. The initial density distribution is first given by that of a nonrotating $n = 1$ polytrope $\rho(z) = \rho_c \sin \pi z / \pi z$. The figure function $s_{2k}(z)$ and total potential $U(z)$ are computed using the ToF5 as described in Zharkov & Trubitsyn (1975) and Ni (2019). In its original version, CEPAM uses an automatic grid refinement method that distributes the grid points in a way that a distribution function of the variables pressure, temperature, mass, radius, and luminosity changes by a constant amount at the grid points. This method requires smooth behavior of the variables and their derivatives. B-splines are used as the interpolating polynomials, which exhibit the desired properties. However, for number of grid points larger than 10^3 , we did not obtain stable solutions with CEPAM. Therefore, for a higher number of grid points we switched to our own solution of the pressure profile using the trapezoidal rule

$$P(z_j) = P(z_{j-1}) + 0.5[\rho(z_j) + \rho(z_{j-1})][U(z_j) - U(z_{j-1})] \quad (6)$$

with the outer boundary condition $P(R_m) = 0$ Mbar. In this case, and in view of the fact that gravitational harmonics show

greater sensitivities to the external levels of a planet, more radial grid points are taken for the outer part: $N/2$ equally distributed over $0.85-1 R_m$ and the other half equally over $0-0.85 R_m$. With CEPAM, we find that this choice yields a modest optimum in accuracy.

Finally, the new density distribution is obtained from the $n = 1$ polytropic EOS $\rho(z_j) = \sqrt{P(z_j)/K}$. This procedure is iteratively performed until all changes in the density distribution are reduced to within a specified tolerance.

In the work of Ni (2020), the gravitational zonal harmonics are calculated as weighted integrals over the internal density distribution $\rho(z)$ using the resulting figure functions $s_{2k}(z)$,

$$J_{2i} = -\frac{2\pi}{MR_{eq}^{2i}} \int_{-1}^{+1} d \cos \theta P_{2i}(\cos \theta) T(R_m, \theta), \quad (7)$$

$$T(R_m, \theta) = \int_0^{R_m} dl \rho(l, \theta) r^{2i+2} \left(\frac{dr}{dl} \right). \quad (8)$$

Using the scaled mean radius $z = l/R_m$ and abbreviating the level surface Equation (4) as $r = zR_m[1 + \Sigma(z, \theta)]$, one can

Table 1
Comparison of the J_{2n} Obtained from Equation (7) and from Equation (5)

Method	$J_2 \times 10^6$	$J_4 \times 10^6$	$J_6 \times 10^6$	$J_8 \times 10^6$	$J_{10} \times 10^6$
Bessel	13 988.51	−531.8281	30.118 32	−2.13212	0.174 07
Equation (7)	13 988.54	−531.8292	30.119 89	−2.13048	0.17446
$ \Delta J_{2i}/J_{2i}^{\text{Bessel}} $	2.42×10^{-6}	1.99×10^{-6}	5.22×10^{-5}	7.67×10^{-4}	2.23×10^{-3}
Equation (5)	13 988.55	−531.8207	30.135 06	−2.10486	0.19555
$ \Delta J_{2i}/J_{2i}^{\text{Bessel}} $	2.52×10^{-6}	1.40×10^{-5}	5.56×10^{-4}	1.28×10^{-2}	1.23×10^{-1}

Note. The numerical values in this table are for a typical number of grid points $N = 2000$ and using the ToF5 coefficients of Zharkov & Trubitsyn (1975). The Bessel solution is taken from Wisdom & Hubbard (2016)

express the function $T(R_m, \theta)$ as

$$T(R_m, \theta) = \frac{3M R_m^{2i}}{4\pi} \left\{ \frac{[1 + \Sigma(1, \theta)]^{2i+3}}{2i+3} \frac{\rho(1, \theta)}{\bar{\rho}} - \int_0^1 dz \frac{[1 + \Sigma(z, \theta)]^{2i+3}}{2i+3} z^{2i+3} \frac{d\rho(z, \theta)/\bar{\rho}}{dz} \right\}. \quad (9)$$

Table 1 shows a comparison of the even harmonics obtained from Equation (7) and from Equation (5) for a typical number of grid points $N = 2000$. The numerical accuracy in J_2 is almost the same for both of them. But the results from Equation (7) are in better agreement with the analytic Bessel-function-based solution for J_4 – J_{10} , where the numerical accuracy for Equation (7) is about 1–2 orders of magnitude better than that for Equation (5).

3.4. Comparison of the J_{2n} of the Uniformly Rotating Polytrope

In Figure 1 we show the relative deviations of the calculated even harmonics from the analytic solutions of Wisdom & Hubbard (2016) as a function of the number N of radial grid points.

With the CEPAM code and ToF5, denoted by 5/Ni in the figure, the numerical accuracy of all the calculated J_{2i} shows good convergence with an increased number of grid points. When the number of grid points is increased beyond $\sim 10^3$, the numerical accuracy in J_4 – J_{10} falls below the current observational uncertainty (Juno D20) reported in Durante et al. (2020). Moreover, the accuracy in all the harmonics J_2 – J_{10} is better than the CEPAM-WH16 results from Guillot et al. (2018), who reportedly applied ToF4, by a factor of roughly 5–100.

Using ToF4 and ToF7 in conjunction with the MOGROP code, denoted by 4/Ne and 7/Ne in the figure, the accuracy significantly improves with denser grid points. Apparently, this code requires a factor of 100 more radial grid points than CEPAM to obtain the same accuracy in J_2 and J_4 . For these low-order harmonics, ToF7 versus ToF5 provides a negligible improvement in accuracy. The situation changes with J_6 . Here, CEPAM with ToF5 levels off at a relative uncertainty of $\sim 5 \times 10^{-5}$, while the higher accuracy of ToF7 versus ToF5 becomes evident as N increases beyond 20,000. However, the typical number of grid points used for planet interior models ranges between 2000 and 4000. For such N values, the numerical accuracy in J_6 with 7/Ne is about the same as the current observational uncertainty reported in Durante et al. (2020). ToF7 begins to pay off with J_8 and higher, even with MOGROP, where J_8 becomes an order of magnitude better than the observational one, 2.5 orders of mag in J_{10} , and 3 orders of mag in J_{12} . We conclude that ToF7 is

sufficiently accurate to address the influence of the winds on J_6 and higher, given current observational uncertainties.

Using the independent TOF-PLANET code of Movshovitz et al. (2020), we obtained similar J_{2n} values to those with the MOGROP code; compare the blue and green lines in Figure 1. In particular, the results for J_4 – J_8 with ToF4 after convergence with grid point number N agree, indicating that the remaining errors $\Delta J_n/J_n$ of 2.5×10^{-4} in J_4 , 10^{-2} in J_6 , and 10^{-1} in J_8 are due to the truncation of the expansion of ToF4. The ToF7 values also agree when convergence is reached, though this applies only to J_{10} and J_{12} for high values of $N > 10,000$. Before convergence with N is reached, the ToF7 errors deviate by a factor of a few, suggesting that the radial grid discretization error matters, which can differ between different implementations even if they use the same trapezoidal rule.

The similar accuracy of MOGROP and TOF-PLANET is due to similar methods for the numerical integration over density (trapezoidal rule) and of the differential equations dm/dr and dP/dr (Runge–Kutta). There is room for improvement. As an example, we extrapolate the J_{2n} values using linear regression on the three solutions for $N = 1000, 2000$, and 4000 for each J_{2n} . In Figure 1, the resulting accuracy is conservatively compared to the result for $N = 9000$, corresponding to the computational cost that scales linearly with N and a small offset for each run. Apparently, the gain in accuracy amounts to two orders of magnitude in J_2 and J_4 , and it is still better than compared to using 10^5 grid points. This suggests that methods other than simply skyrocketing the number of grid points may help to improve the accuracy of numerical J_{2n} computations.

We note that at present ToF is entirely outperformed by the CMS method with regard to accuracy. Militzer et al. (2019) reported relative inaccuracies of only 7.3×10^{-9} in J_2 , 2.1×10^{-10} in J_4 , 3.6×10^{-8} in J_6 , 4.2×10^{-8} in J_8 , 1.1×10^{-7} in J_{10} , and 6.7×10^{-9} in J_{12} for $N = 2^{17} = 131,072$ CMS layers, out of which only 512 are treated explicitly, while the shape of intermediate ones is obtained by interpolation.

4. Application to Jupiter

4.1. Jupiter Models

The models of this work assume a four-layer structure. By Y_i we denote the helium mass fraction in layer number i with respect to the H/He system. Layer 4 is a compact rocky core. Layer 1 is an atmosphere with a helium mass fraction of $Y_1 = 0.238$ as measured by the Galileo entry probe. Layers 2 and 3 have the same helium abundance ($Y_2 = Y_3$), which is adjusted to yield an overall helium mass fraction $Y = 0.2700(4)$. A possible He-rain region in Jupiter is represented by a jump in helium abundance between layers 1 and 2. Transition pressures of 1–4 Mbar for P_{12} are considered, which are typical pressures where the Jupiter

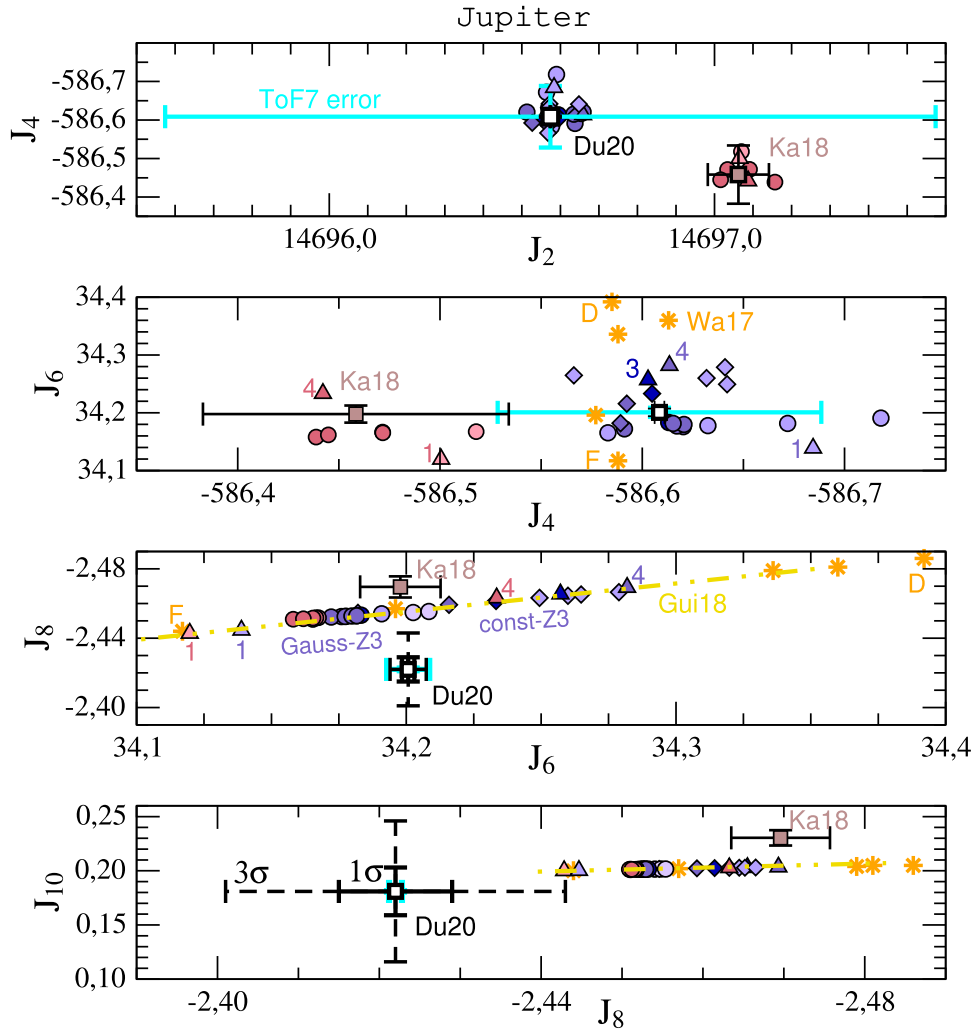


Figure 2. J_{2n} values scaled by 10^6 , observed by Juno (white squares), corrected for latitude-dependent winds (brown squares; Kaspi et al. 2018), models with MH13 EOS (orange stars; Wahl et al. 2017b), models in Extended Data Figure 1 of Guillot et al. (2018; yellow), models with CMS-19 H/He EOS and $P_{12} = 1, 3, 4$ Mbar (triangles), $P_{12} = 2$ Mbar and P_{23} varied from 5 to 20 Mbar, and constant Z_3 (diamonds) or Gaussian Z_3 (circles). All J_{2n} values are multiplied by 10^6 .

adiabat reaches the closest point to the H/He demixing boundary of H/He phase diagrams for protosolar H/He ratios as predicted by first-principles simulations (Lorenzen et al. 2011; Morales et al. 2013; Hubbard & Militzer 2016; Schoettler & Redmer 2018). Adjusting the local He abundance to the local P - T conditions along the phase boundary yields an approximately linear increase in Y ; however, the gradient and width of the He-rain region depend on the temperature profile assumed therein (Nettelmann et al. 2015), which may range in Jupiter from adiabatic to modest superadiabaticity (Mankovich & Fortney 2021). A recent analysis of reflectivity data obtained for H/He samples that were pre-compressed to 2–4 GPa in diamond anvil cells and further shock-compressed to 60–180 GPa using the OMEGA layer indicates that an even larger portion of the Jupiter adiabat may intersect with the H/He phase boundary, as at the highest pressure where evidence of demixing is seen, 150 GPa, the measured temperatures were 10,000 K (Brygoo et al. 2021). Assuming a flat $T(P)$ phase curve at Mbar pressures, such a temperature corresponds to ~ 8 Mbar along the Jupiter adiabat (Hubbard & Militzer 2016).

Although He droplets may carry specific elements such as Ne with them downward (Wilson & Militzer 2010) and affect the

metallicity between the He-depleted outer and He-enriched inner regions, we assume constant heavy-element mass fractions across that boundary ($Z_1 = Z_2$). Finally, between layers 2 and 3, the heavy-element mass fraction is allowed to change. We use either a constant Z_3 value, implying a jump in Z at a transition pressure P_{23} , or a Gaussian- Z_3 profile that starts with $Z(P_{23}) = Z_2$ and smoothly increases toward a maximum $Z_{3,\max}$ at $P = 38$ Mbar near the core. The choice of 38 Mbar is arbitrary and was taken to be just above the usual core–mantle boundary pressures, which are found to be around 40 Mbar in Jupiter. The two free parameters in that setup to adjust J_2 and J_4 are Z_1 and Z_3 or $Z_{3,\max}$.

We employ the CMS-2019 EOSs for H and He (Chabrier et al. 2019) and mix them with the water EOS H₂O-REOS with respect to density only. The T - P profile is that of the H/He adiabat, which begins at $T = 166.1$ K at 1 bar. We construct curves of constant entropy (adiabats) by using the specific entropy values $s_H(P, T)$ and $s_{He}(P, T)$ provided in the tables for hydrogen and helium (Chabrier et al. 2019) after adding a composition-dependent entropy of mixing term $s_{\text{mix}}(X_{H_2}, X_{He})$. For the concentrations, we assume that helium is nonionized and that hydrogen is either molecular or ionized, taking the degree of ionization as in Nettelmann et al. (2008). Since we found these H/

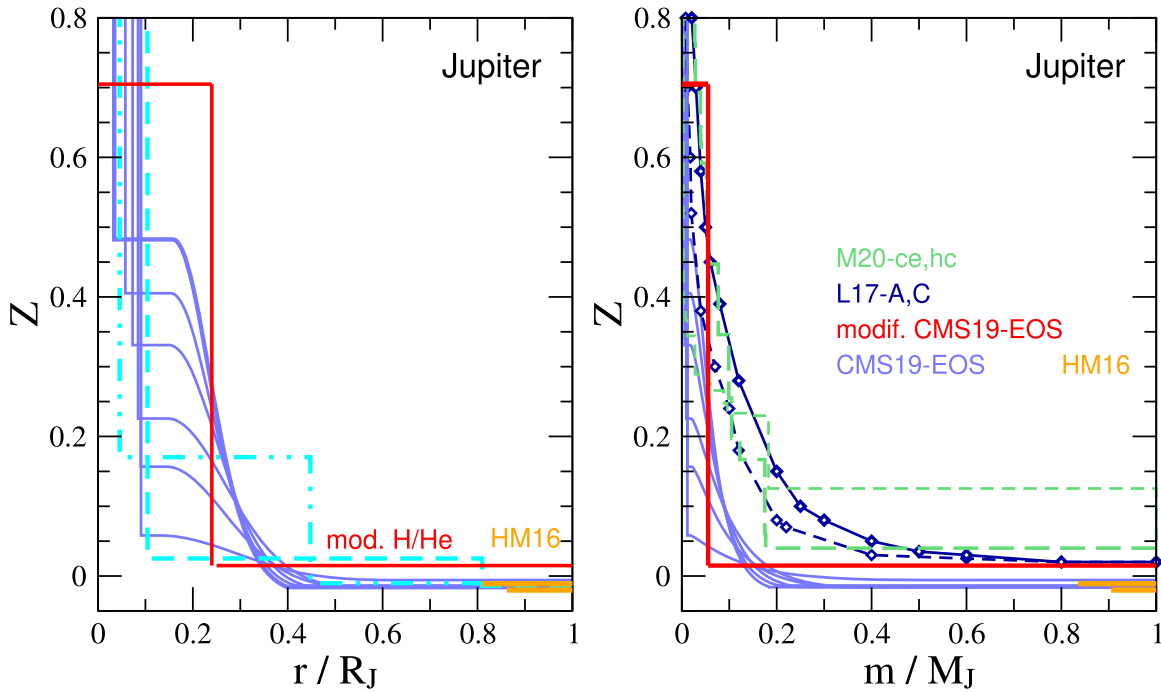


Figure 3. Internal heavy-element abundance profiles over radius (left panel) and over mass (right panel) of some of the Jupiter models in Figure 2 with Gaussian Z_3 (blue), with constant Z_3 (cyan), and for a model with $\rho(P)$ along the adiabat modified to yield $1 \times$ solar Z (red). Overplotted are the outer envelope Z -level of model DFT-MD7.15 from Hubbard & Militzer (2016) (orange), the $Z(m)$ profiles of the formation models A and C (dark blue) of Lozovsky et al. (2017) at the final stage of mass accretion, after settling but before possible homogenization by mixing, and $Z(m)$ profiles of Müller et al. (2020) for their envelope accretion models assuming a hot-compact or a cold-extended state at the onset of gas accretion (green).

He adiabats to be too dense to yield Jupiter models with nonnegative atmospheric metallicity, we also perturb that adiabat toward lower densities as described in Section 4.3.

4.2. Results for Jupiter’s Even Harmonics

In Figure 2 we show the even J_2 – J_{10} values from rigidly rotating Jupiter models. Models adjusted to the Juno observations of J_2 and J_4 (Durante et al. 2020) are shown in bluish color, while models adjusted to the wind-corrected J_2 and J_4 values by the corrections of Kaspi et al. (2018) applied to the J_2 , J_4 values of Durante et al. (2020) are shown in reddish color.

Due to imperfect fit to the J_2 , J_4 values, the scatter in model J_2 and J_4 values is larger than the observational uncertainty. For J_4 , the scatter $\Delta J_4 / J_4$ is about $\pm 2 \times 10^{-4}$ and of the same size as the relative uncertainty due to using ToF7 in the MOGROP code, while for J_2 the latter relative uncertainty is with 7×10^{-5} overwhelming. Still, these relative deviations are too small to matter for the inferred metallicities. Guillot et al. (2018) allowed for a similarly wide scatter in J_2 model values of $\pm 3.4 \times 10^{-5}$ and a wider scatter in J_4 of $\pm 10^{-3}$ relative deviations. They found that, nevertheless, the high-order moments J_8 versus J_6 and J_{10} versus J_8 were strictly confined to a straight line. We confirm that behavior.

Notably, the model $|J_8|$ values are higher than the observed value, and a trend in that direction is also seen for J_{10} , although the model J_{10} values are still within the 3σ observational uncertainty. Wind models assuming rotation along cylinders indeed predict a slight decrease in $|J_8|$ and J_{10} if the observed wind profile of the southern hemisphere is applied to the entire surface, while they predict an enhancement if the wind profile of the northern hemisphere is used (Hubbard 1999). The wind model by Kaspi et al. (2018) that was adjusted to explain the odd moments of Jupiter observed by Juno yields a correction

qualitatively in the direction as predicted for the southern winds and seen in the model values for rigid rotation, albeit quantitatively stronger by a factor of two. This deviation may have many reasons; clearly, further exploration of the connection between interior and wind models is desirable.

For J_6 , the uncertainties from the application of ToF7 in the MOGROP code, from observations, and from the wind contribution are all small and of the same size. In contrast, model assumptions such as the location of layer boundaries not only have a larger influence on J_6 but also yield a scatter around the observed value. Hence, we conclude that Jupiter’s J_6 is unique in that it neither is adjusted nor seems to be significantly influenced by the winds, and therefore it offers an additional parameter to further constrain interior models. We find that models with a Gaussian Z_3 and an abrupt He-poor/He-rich transition at $P_{12} = 1$ – 2 Mbar yield $J_6 = (34.11$ – $34.18) \times 10^{-6}$, slightly below the observed value, while models with that transition deeper inside at $P_{12} = 2.5$ – 3 Mbar yield $J_6 = (34.23$ – $34.28) \times 10^{-6}$, slightly above the observed value. Constant- Z_3 profiles and $P_{12} = 2$ Mbar stretch from $J_6 = (34.18$ to $34.28)$ times 10^{-6} around the observed value $(34.2007 \pm 0.0067) \times 10^{-6}$ upon shifting P_{23} from 5 Mbar deeper down to 18 Mbar. Taken at face value, Jupiter’s observed J_6 value indicates that the He-depleted/He-enriched transition occurs at around 2–2.5 Mbar.

4.3. Z Profiles for Jupiter

In Figure 3 we show the radial heavy-element distribution of some of the models with Gaussian Z in layer No. 3. Models with unmodified H/He adiabat appear in light blue and are described in Section 4.3.1, while models with modified H/He adiabat appear in red and are described in Section 4.3.2.

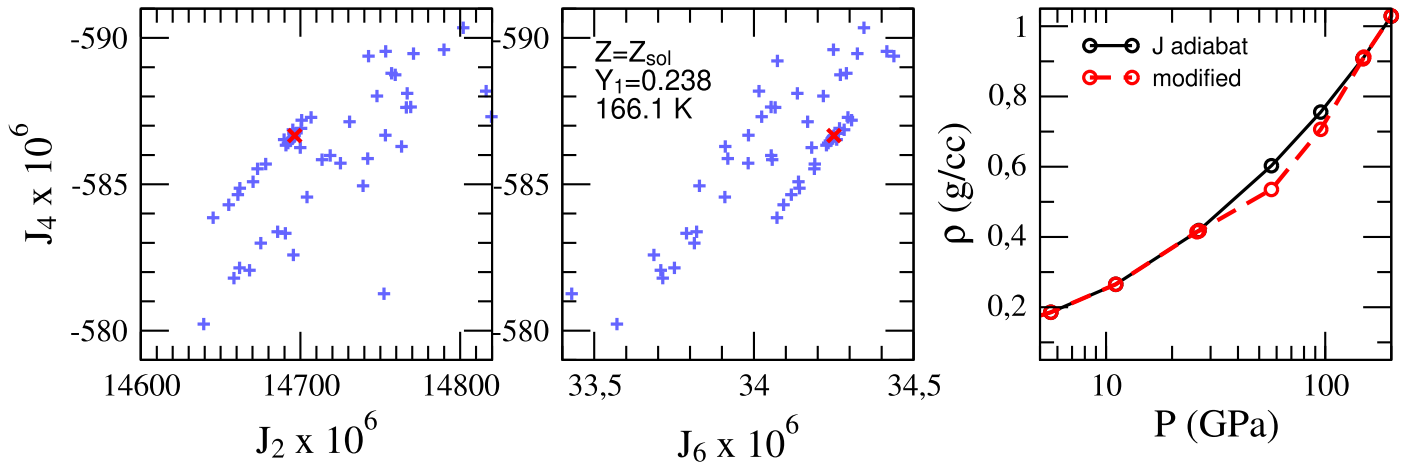


Figure 4. J_2 – J_4 (left) and J_6 – J_4 (middle) values of three-layer models with $Z_1 = 1 \times$ solar and modified Jupiter adiabats. Only the red-highlighted model meets the Juno constraints. Its adiabat is shown in the right panel (red curve).

4.3.1. Unmodified H/He Adiabats

All our models with CMS-19 EOSs that fit J_2 and J_4 have negative Z_1 values between -0.005 and -0.020 (-0.33 to $-1.33 \times$ solar). This is consistent with Hubbard & Militzer (2016), who obtained $-0.6 M_E$ of heavy elements in the molecular region for their MH13 EOS-based model DFT-MD7.15, which, with $J_4 = 587 \times 10^{-6}$, is the one that comes closest to the Juno value of -586.61×10^{-6} . For a conservative estimate of their Z_1 value we take 1 Mbar, the entry of their Jovian adiabat into the H/He demixing boundary of Morales et al. (2013), or 2 Mbar, the pressure medium in their H/He-rain region. With a corresponding molecular envelope mass of $\sim 30 M_E$ and $\sim 53 M_E$, respectively, we obtain Z_1 between -0.011 and -0.02 for model DFT-MD7.15. In contrast, Debras & Chabrier (2019) found a variety of models for nonnegative atmospheric Z values of $1 \times Z_{\text{Gal}} = 0.0167$ using CMS-19 H/He EOSs. We cannot reproduce the results of Debras & Chabrier (2019) quantitatively.

The deeper the layer boundary for heavy elements is placed, the higher will the deep interior heavy-element abundance become, and the smaller the core mass (Nettelmann et al. 2012). With CMS-19 EOSs, the response of M_{core} to P_{23} is comparably weak, so that P_{23} can be placed as deep as 20 Mbar before the compact core disappears. The thick blue model in Figure 3 is for $P_{23} = 21$ Mbar and has a core mass of only $0.25 M_E$.

The nonexclusive compact core mass values of our models range from 0.2 to $4.8 M_E$ for $P_{12} = 2$ Mbar and Gaussian- Z envelopes, from 0.6 to $6.0 M_E$ for constant- Z envelopes, and from 1.2 to $3.8 M_E$ for wind-corrected models.

For Gaussian- Z deep envelopes, $Z_{3,\text{max}}$ can become quite large toward the center. We obtained $Z_{3,\text{max}}$ values up to 0.5 , although larger values may be possible if the maximum of the Gaussian curve is placed at the center, while we placed it slightly off at 38 Mbar.

The mass of heavy elements in the deep interior below the negative- Z envelope amounts to 7.5 – $10.1 M_E$. Assuming a $1 \times$ solar instead of negative- Z envelope would add another $3.8 M_E$ of heavy elements. A total of 11.3 – $13.9 M_E$ of heavy elements is consistent with the Jupiter core accretion formation models A and C of Lozovsky et al. (2017). These models assume solid surface densities of 6 and 10 g cm^{-2} and planetesimal sizes of 100 and 1 km , respectively. Lozovsky et al. (2017) find that a

total amount of heavy elements of $9.3 M_E$ (A) and $16.4 M_E$ (C) is accreted. Correspondingly, for the average Z value after final mass accretion, Helled & Stevenson (2017) find $\sim (0.03$ – $0.05) \times M_J = 9.5$ – $16 M_E$ of heavy elements for model A and a third model D, which assumes a solid surface density of 10 g cm^{-2} like model C. In Figure 3, models A and C are shown after settling of heavy elements but before possible convective mixing. Settling takes place if the partial pressure of ablated incoming material exceeds its vapor pressure. The resulting $Z(m)$ profiles after formation resemble our interior models with Gaussian Z_3 , although the Z gradient in the post-formation models begins farther out at $\sim 0.5 M_J$ than at ~ 0.2 – $0.3 M_J$ as in our models. On the other hand, a shallow, primordial compositional gradient has been found to erode and to be erased in present Jupiter if vigorous convection takes place in the envelope (Müller et al. 2020), while a steep compositional gradient may still persist within $0.2 M_J$. The present-state models for Jupiter of Müller et al. (2020) are similar to our models with either Gaussian Z_3 or constant Z_3 when the heavy-element-enriched deep interior (or dilute core) is assumed to begin deep inside at > 15 Mbar, except that our models underestimate the outer envelope metallicity while the evolution models of Müller et al. (2020) overestimate it, as they yield too small a present-day radius.

4.3.2. H/He Adiabats Modification

Models with negative Z values are, needless to say, not considered a viable solution. There are two obvious ways how negative Z values in the atmosphere and outer envelope can be circumvented. One possibility is to assume a superadiabatic region above the region where J_4 is most sensitive, which—for a polytropic Jupiter model—is in the molecular envelope at around 50 GPa ($0.9 R_J$). A superadiabatic temperature profile may result from stable stratification. Christensen et al. (2020) showed that meridional flows in a stably stratified, slightly conducting region slow down the strong zonal flows and suggested the existence of such a region in Jupiter as an explanation for the truncation of the zonal flows, which, according to recent combined analysis of magnetic field and gravity field data, occurs rather sharply at $0.97 R_{\text{Jup}}$ (Galanti & Kaspi 2021).

However, stable stratification does not necessarily result in a superadiabatic temperature profile. Depending on its origin,

stable stratification can also be accompanied by a subadiabatic temperature profile. For instance, in the absence of alkali metals the opacity of the H/He fluid becomes sufficiently low for the intrinsic heat to be transported by radiation along a subadiabatic radiative gradient (Guillot et al. 1994, 2004), leading to subadiabatic stable stratification according to the Schwarzschild criterion. Superadiabatic gradients are predicted in a Ledoux-stable, inhomogeneous medium of upward-decreasing mean molecular weight. Clouds formed by condensibles of higher molecular weight than the background composition can induce Ledoux stability if their abundance is high enough. Such a scenario has been proposed for the presumably water-rich atmospheres of the ice giants (Leconte et al. 2017). Water clouds may occur in Jupiter at 100 bars, and silicate clouds at 1000 bars, both below the level that so far could be probed by the Galileo entry probe (22 bars) and Juno MWR remote sensing (Li et al. 2020). Therefore, clouds are candidate causes for superadiabatic stable stratification.

Another possibility to avoid negative metallicities is to perturb the H/He adiabat toward lower densities. The CMS-19 hydrogen EOS shows excellent agreement with a variety of experimental data ranging from shock compression experiments for H and D at various initial conditions to isentropic compression (Chabrier et al. 2019). At 50 GPa, the H EOS is even slightly stiffer than the experimental data. Only the helium EOS shows significantly higher densities in the 20–150 GPa area than inferred from the shock compression experiments (Chabrier et al. 2019). Although the good agreement between the theoretical P – ρ relations and the experiments, as well as between CMS-19 H/He adiabats and MH13 EOS adiabats, is far from suggesting that the CMS-19 H/He EOS would significantly overestimate the density along the Jupiter adiabat, we here perturb it toward lower densities. We conduct a three-parameter study where we vary the maximum deviation $\delta\rho_{\max}$, the pressure entry point P_{start} , and the pressure exit point P_{end} . Between P_{start} and P_{end} , $\delta\rho$ adopts its maximum at the logarithmic mean pressure value and is otherwise linearly interpolated as $\delta\rho(\log P)$. We explore P_{start} values between 1 and 50 GPa and P_{end} values between 50 and 150 GPa. The smaller P_{start} and P_{end} , the lower the $|J_4|$ and $|J_4|/J_2$ ratio. We find $P_{\text{start}} \leq 30$ GPa necessary in order to have a noticeable influence on J_4 . Conversely, higher P_{end} values lead to a stronger reduction on J_2 . The question we ask is, for what values of $\delta\rho$, P_{start} , and P_{end} can a model be found with a $1 \times$ solar homogeneous Z ?

For a homogeneous, unperturbed adiabat at $Y_1 = 0.238$ and Y_2 adjusted to meet $Y = 0.27$, both $|J_4|$ and J_2 turn out to be significantly too large. This is in contrast to the result by Debras & Chabrier (2019), who could match J_2 at $1 \times Z_{\text{Gal}}$. Thus, we need P_{start} to be sufficiently low for J_4 and P_{end} sufficiently high for J_2 . We find such an optimized solution for $P_{\text{start}} = 26$ GPa, $P_{\text{end}} = 150$ GPa, and $\delta\rho = -0.1257$, i.e., a maximum reduction of the H/He adiabat by 12.57%. The resulting P – ρ profile is shown in Figure 4(c), while the ensemble of models in the J_2 – J_4 and J_6 – J_4 space is shown in Figures 4(a) and (b). Notably, among the wide spread of intermediate models in the J_2 – J_4 – J_6 space, the one model (red cross) that meets the Juno J_2 , J_4 values yields $J_6 = 34.20 \times 10^{-6}$, in excellent agreement with the Juno observation. For this model, the total Z amounts to $15.6 M_{\oplus}$, in good agreement with the formation model of Lozovsky et al. (2017). This

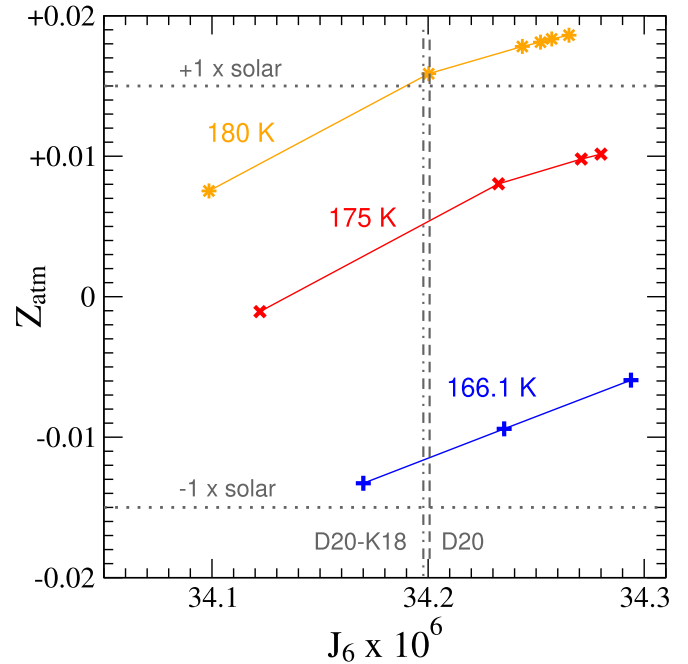


Figure 5. Outer-envelope heavy-element mass fraction (water) and J_6 values of Jupiter models with 1 bar temperature of 166.1 K for transition pressures from left to right of $P_{12} = 2, 3, 6$ Mbar (blue); 175 K for P_{12} of 2, 6, 8, 8.5 Mbar (red); and 180 K for P_{12} of 2, 6, 8–10 Mbar (orange). The models are calculated using the unmodified H/He CMS-19 EOS and fit the wind-corrected J_2 , J_4 values using the corrections of Kaspi et al. (2018). Horizontal dotted lines indicate $\pm 1 \times$ solar metallicity $Z_{\text{solar}} = 0.015$, while vertical lines indicate the observed J_6 value of Durante et al. (2020; dashed) and its wind-corrected value (dotted-dashed).

exploration suggests that winds on Jupiter have a negligible influence on J_6 .

4.3.3. Models for Enhanced 1 bar Temperature

In this section, we present Jupiter models for $T_{1\text{bar}} = 175$ K and $T_{1\text{bar}} = 180$ K. Here, we do not modify the adiabat or EOS, and we adjust the J_2 , J_4 model values to the wind-corrected observed values using the corrections of Kaspi et al. (2018).

Such warmer models are not preferred, first, because these 1 bar temperatures significantly exceed the Galileo entry probe measurement of 166.1 K. This would not have posed a problem if a mechanism had been studied that predicted a superadiabatic region underneath the 22 bar region, wherein temperatures and thus entropy would rise to the level corresponding to these or even higher 1 bar temperatures. Clouds may have a warming effect if they stabilize the region of condensation (Leconte et al. 2017); however, latent heat release from condensation opposes this effect and leads to a cooler interior underneath the cloud region, as has been discussed for ice giant atmospheres (Kurosaki & Ikoma 2017). Second, Jovian adiabats for different H/He EOSs tend to intersect with H/He demixing curves at best in a small region at 1–3 Mbar. At present, only the rather cool MH13 EOS-based Jupiter adiabat for 166.1 K shows a clear intersection by about 450 K (Hubbard & Militzer 2016) with the state-of-the-art first-principles-based H/He demixing curve of Morales et al. (2013), while the intersection with the lower demixing curve $T_{\text{dmx}}(P)$ of Schoettler & Redmer (2018) is only marginal (Mankovich & Fortney 2021). Since enhancing $T_{1\text{bar}}$ from the Galileo value of 166.1 K by only 14 K leads to an enhancement by ~ 350 K at 1

Mbar and even by 460 K at 2 Mbar according to our CMS-19 EOS-based Jupiter adiabats, higher surface temperatures might let the demixing region in Jupiter entirely disappear. We stress that although our CMS-19 Jupiter adiabat for $T_{1\text{ bar}} = 166.1$ is rather dense, it is also rather warm and, with 5700 K at 1 Mbar and 6840 K at 2 Mbar, outside of the first-principles-based demixing regions (Morales et al. 2013; Schoettler & Redmer 2018).

On the other hand, the recent experimentally predicted phase boundary inferred from an observed upward jump in reflectivity at 0.93 Mbar and downward jump at 1.5 Mbar, which are interpreted as the entry and exit of the compressed H/He sample in and out from the demixing region (Brygoo et al. 2021), suggests high demixing temperatures of 10,000 K. Primarily it is this finding that motivates us to allow for higher surface temperatures and for higher transition pressures, which we allow to reach the maximum where the core mass disappears, or for practical reasons drops below $1 M_E$.

In Figure 5 we show the resulting outer envelope metallicity Z_{atm} and J_6 values. Obtaining $1\times$ solar metallicity requires $T_{1\text{ bar}}$ of 180 K (orange curve) or higher. While not negligible, additional uncertainties in the atmospheric helium abundance and J_4 are small and not considered here. Notably, for $T_{1\text{ bar}} = 180$ K and at the transition pressure between the He-poor and He-rich regions at $P_{12} = 6$ Mbar, we obtain $1\times$ solar metallicity throughout the interior down to $\sim 0.4R_J$, thus a largely solar-metallicity envelope. At 6 Mbar, the temperature amounts to 10,400 K and is thus at the upper limit of the experimentally inferred demixing temperature (Brygoo et al. 2021). For that model, the static J_6 value is consistent with the observed value and its small wind correction according to Kaspi et al. (2018). As is well known (Nettelmann et al. 2012), Z_1 rises with P_{12} .

If there were no uncertainties in the H/He EOS, these models would suggest that the internal Jupiter adiabat lies at higher entropy than the observed adiabat down to 22 bars, and that Jupiter's envelope metallicity is not much higher than $1\times$ solar.

5. Application to Saturn

5.1. Saturn Models

The Saturn models of this work are built in the same manner as the Jupiter models described in Section 4.1, although in the real planets, helium rain may induce a dichotomy (Mankovich & Fortney 2021). We fit the Saturn models to the observed J_2 , J_4 values without accounting for the wind corrections. We assume that a rotation rate of 10:32:45 hr, as suggested by Helled et al. (2015), would yield a best match of interior models to the observed pre-Cassini Grand Finale gravity and Pioneer and Voyager shape data. Within the given uncertainty of 46 s, this value is consistent with the more recently suggested rotation rates of 10:33:34 hr (Militzer et al. 2019), using the Cassini Grand Finale gravity and the same shape data, and with the rotation rate of $10:33:38 \text{ hr}^{+1m52s}_{-1m19s}$ inferred from the comparison of Saturn ring wave frequencies observed by Cassini with theoretical predictions for f -mode frequencies as a function of the planet's rigid-body rotation rate (Mankovich et al. 2019). We set the 1 bar surface temperature to 135 K in accordance with the Voyager measurement of 135 ± 5 K (Lindal 1992). The outer boundary is placed at a reference

radius for the J_n of 60,330 km, which corresponds to the 0.1 bar level.

Saturn's atmospheric He abundance can be considered poorly known, as different estimates only agree in finding depletion compared to the protosolar value $Y_{\text{proto}} \sim 0.27$ but disagree about the level of depletion. The lowest estimate $Y_1 = 0.06 \pm 0.05$ stems from a combined Voyager radio occultation and infrared spectra analysis (Conrath et al. 1984), while the highest estimate $Y_1 = 0.18\text{--}0.25$ stems from a reanalysis of only the Voyager infrared data (Conrath & Gautier 2000). More recent Cassini-data-based estimates fall in between, ranging from $Y_1 = 0.075\text{--}0.13$ from Cassini infrared remote sensing (Achterberg & Flasar 2020) to $Y_1 = 0.158\text{--}0.217$ from Cassini stellar occultations and infrared spectra (Koskinen & Guerlet 2018). A low value of 0.07 ± 0.01 is independently inferred from shifting the most recent H/He phase diagram of Schoettler & Redmer (2018) to reproduce the He abundance measurement by the Galileo entry probe on Jupiter, in conjunction with the MH13 H/He EOS and adiabat (Mankovich & Fortney 2021). When the same procedure is applied to the H/He phase diagram of Lorenzen et al. (2011) in conjunction with the SCvH-H/He EOS, which both are now outdated, the yield is $Y_1 = 0.13\text{--}0.16$ (Nettelmann et al. 2015), in between the most recent observational estimates (Achterberg & Flasar 2020; Koskinen & Guerlet 2018). Here we construct models for the two moderate depletion values $Y_1 = 0.14$ and $Y_1 = 0.18$ using the CMS-19 EOS and allow for a wider spread of $0.06\text{--}0.18$ when using the modified CMS-19 adiabat. For comparison, Galanti et al. (2019) used $Y_1 = 0.18 \pm 0.07$, Militzer et al. (2019) used $Y_1 = 0.18\text{--}0.26$, and Ni (2020) used $Y_1 = 0.12\text{--}0.23$. Lower Y_1 values yield higher atmospheric and higher maximum deep interior metallicities (Militzer et al. 2019; Ni 2020).

Saturn thermal evolution models with H/He phase separation and helium rain predict that in Saturn helium rains down to the core, forming an He-rich shell of 0.90–0.95 mass percent helium atop the core (Püstow et al. 2016; Mankovich & Fortney 2021). If the helium abundance between the onset pressure of H/He phase separation and the He shell follows an H/He phase diagram, it increases gradually with depth. However, these thermal evolution models assume for simplicity a constant low envelope metallicity. How deep He droplets can sink in a high- Z and thus higher-density deep interior, as predicted by Saturn models constrained by gravity and ring seismology data (Mankovich & Fuller 2021), remains to be investigated. For simplicity, we here represent the He gradient by a jump in the He abundance at a pressure of $P_{12} = 2\text{--}4$ Mbar deep within the He-rain region, for which predicted onset pressures in present Saturn range from 0.8 Mbar (Militzer et al. 2019) to 2 Mbar (Mankovich & Fortney 2021). Below P_{12} , we keep the He/H ratio constant with depth.

Typical core-envelope pressures are around 15 Mbar. We vary P_{23} between 4 and 7 Mbar and let the Gaussian- Z_3 profiles adopt its maximum at 12 Mbar if the core is compact ($Z = 1$) or farther out at 6–12 Mbar if the core is dilute and thus more extended. Dilute cores are created by setting $Z = 0.6\text{--}0.7$ in the core, the remaining constituent being the H/He/ Z mix from envelope layer No. 3 above.

5.2. Results for Saturn's Even Harmonics

Figure 6 shows the even J_n values from our Saturn models, from the two Saturn models of uniform rotation (UR) in less

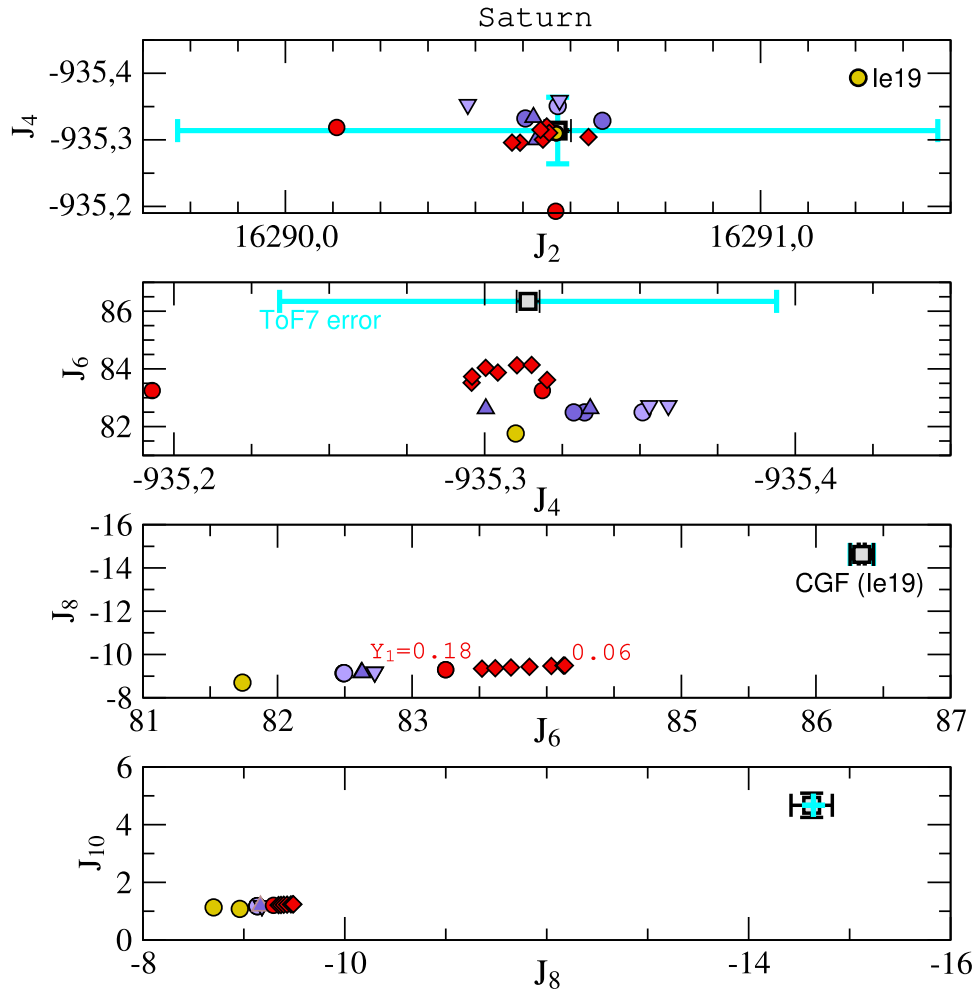


Figure 6. J_{2n} values multiplied by 10^6 for Saturn: Observed J_{2n} values from the Cassini Grand Finale (CGR; gray squares; Iess et al. 2019), ToF7 uncertainties are overplotted to the observed values (cyan), interior model results assuming uniform rotation between 10h32m44s and 10h47m06s (Iess et al. 2019; golden). This work’s models: blue upward-pointing triangles: adiabatic, $Y_1 = 0.14$, Gaussian Z_3 ; blue downward-pointing triangles: adiabatic, $Y_1 = 0.14$, constant Z_3 ; blue circles: $Y_1 = 0.18$, superadiabatic; red circles: modified H/He adiabat, dilute core, $Y_1 = 0.18$; red diamonds: modified H/He EOS and Y_1 between 0.16 and 0.06, dilute core, Gaussian Z_3 .

et al. (2019), and from the Cassini Grand Finale observed values (Iess et al. 2019). Unlike the case of Jupiter, Saturn’s observed even $|J_n|$ values are clearly enhanced over the model predictions for $n \geq 6$. The enhancement can be explained by rotation along cylinders that rotate approximately but not exactly with the observed speeds of clouds in the equatorial region and midlatitude region up to $\pm 40^\circ$ (Militzer et al. 2019). The observed J_n can also be explained by a thermal wind if a little deviation of the deeper wind speeds from the cloud speeds is allowed (Galanti et al. 2019). The enhancement of the even J_n by the zonal winds is quite substantial. Already for J_6 , we find a 4.2%–5.3% influence, although it diminishes to 2.4%–3.7% for the modified adiabat. Iess et al. (2019) obtain slightly lower UR model J_6 values and a 5.5% effect, while Galanti et al. (2019), who allow for a much wider scatter in model J_4 values of $\pm 40 \times 10^{-6}$, obtain UR model J_6 values up to 87×10^{-6} , which encompasses the observed value. However, the mean of their distribution for fast, uniform rotation lies at 82×10^{-6} , implying a 5.5% influence of the winds on J_6 , consistent with this work. The strong influence of the winds seen in J_6 suggests that also J_4 and J_2 are affected by the winds. In Section 6, we investigate whether the observed winds are

consistent with a smaller influence on J_6 than found in previous work (Iess et al. 2019).

5.3. Z and ρ Profiles for Saturn

Saturn interior models allow for higher atmospheric metallicities than Jupiter interior models when using the same H/He EOS. For instance, Nettelmann et al. (2013) obtains $1.5\text{--}6 \times$ solar for Saturn and fast rotation of 10:32:00 hr, but only $0\text{--}2.5 \times$ solar for Jupiter when applying H-REOS.2 EOS. Wahl et al. (2017b) obtained only $0\text{--}0.7 \times$ solar for Jupiter using MH13 EOS, while Militzer et al. (2019) obtained $1\text{--}4 \times$ solar for Saturn, consistent with Ni (2020), who obtained $0\text{--}6 \times$ for Saturn by considering a wide range of atmospheric He abundances, rotation rates, and wind corrections.

Here we obtain $Z_1 = 0.02\text{--}0.06$ ($1.5\text{--}4 \times$ solar) for nominal He abundances Y_1 of 0.14–0.18, and we obtain compact nonexclusive core masses of $5\text{--}8.6 M_E$, meaning that solutions with lower core masses are expected to be possible for deeper transition pressures than considered here. Representative Z and ρ profiles are shown in Figure 7. Compact rocky cores yield higher central densities than suggested by the 16th–84th percentile probability range of models of Movshovitz et al. (2020),

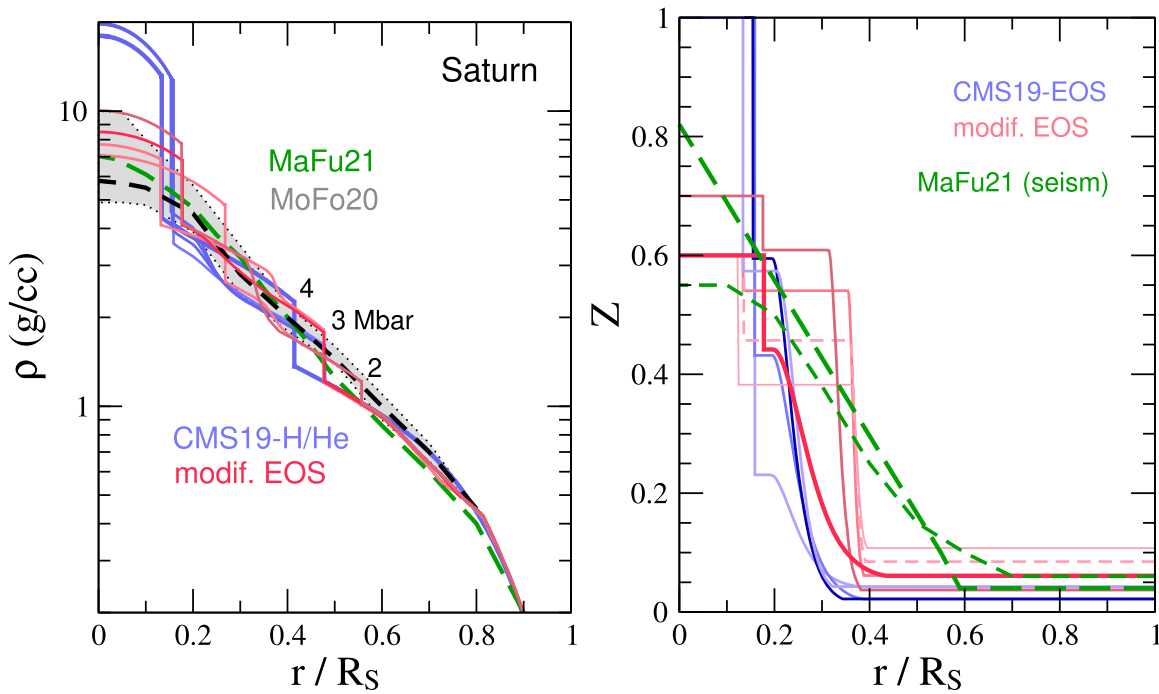


Figure 7. Density profiles (left panel) and radial Z profiles (right panel) of Saturn models with a compact core (blue) or a dilute core of $x_R = 0.6$ – 0.7 and using the Jupiter-optimized adiabat (red), approximate 2σ -likelihood distribution of Movshovitz et al. (2020; gray), and likelihood mean from seismic constraints (green) adapted from Mankovich & Fuller (2021) assuming a linear $Z(r)$ (thick dashed) or a sigmoidal $Z(r)$ (right panel only). The highest atmospheric Z levels of the red curves are for lowest atmospheric $Y = 0.06$.

which are constrained by the gravity data. The latter models agree well with density distributions with inhomogeneous Z profiles constrained by Cassini ring seismology data (Mankovich & Fuller 2021). However, we were not able to find a model with a low-density core and the original H/He EOS, as such cores extend far out and yield J_2 values that are too large. Applying the same modification to the Saturn adiabat as for the Jupiter-optimized adiabat (see Section 4.3.2), we are able to obtain Saturn models with extended, low-density cores, in agreement with the likelihood distributions. As we mix H/He, with little addition of ice, into the rocky core region, we need rather high H/He amounts of 30%–40% by mass (Figure 7, right panel) to reduce the core densities to 6 – 7 cm^{-3} (left panel). This is consistent with Mankovich & Fuller (2021), who need 30%–40% of H/He for rocky cores but only 0%–10% for icy cores. When also allowing the atmospheric He abundance to decrease down to 0.06, we obtain up to $7 \times$ solar atmospheric Z .

Even in our dilute core models, the high- Z part is concentrated in the innermost $0.4 R_{\text{Sat}}$ at pressures above 4 Mbar. For comparison, seismic constraints are required (Mankovich & Fuller 2021) to extend the Z -gradient zone, depending on the assumed functional form of $Z(r)$, out to 0.6 – $0.7 R_{\text{Sat}}$, where the pressure is around 1 Mbar. While we did not explore such extended Z gradients in order to keep them separated from the He-gradient zone, which we placed at 2 – 4 Mbar, this comparison suggests that in the real Saturn heavy-element and helium gradients overlap. Together, the Z and He abundance profiles of our models suggest that the compositional gradient required to explain the ring seismology data could be due to both a diffuse core (inner region) and helium rain (outer region).

In comparison to Jupiter, the total amount of heavy elements is clearly higher in Saturn. Models with the unperturbed H/He

adiabat yield $M_Z \sim 12.6$ – $13.6 M_E$ for Saturn and 7.5 – $10.1 M_E$ for Jupiter (Section 4.3.1). Lower densities along the H/He adiabat and warmer interior temperatures would increase these values.

6. Including the Zonal Wind Profiles

Our Jupiter models with a modified or unmodified H/He adiabat allow for a largely homogeneous interior down to $0.4 R_J$ with a small rock core (Figure 3) and for J_6 unaffected by the winds (Figure 2). Our Saturn models allow for larger static J_6 values in the range $(82.5$ – $84.0) \times 10^{-6}$ than previous work (81.8×10^{-6}); see Figure 6.

Here we investigate whether such models for Jupiter and Saturn are consistent with the observed wind profiles and odd and even J_n values. We pick one representative Jupiter model (unmodified adiabat, $P_{12} = 2$, $P_{23} = 20$ Mbar, compact core of mass $1.26 M_E$) and the Saturn model highlighted in red in Figure 7 (modified H/He adiabat, dilute core, $Y = 0.14$).

The wind modeling approach is the same as described in Galanti & Kaspi (2021), except that the Saturn rotation period to which the wind speeds refer is adjusted to the value of the interior model, $10\text{h}32\text{m}45\text{s}$. We use either only the gravity data to constrain the wind decay depth profiles, as in Kaspi et al. (2018) and Galanti et al. (2019), or both the gravity and magnetic field data combined (grav+MHD), as in Galanti & Kaspi (2021). As an uncertainty in the static J_{2n} values we take the Tof7 errors produced by MOGROP for $N = 4000$.

With this approach, we are able to find fits that reproduce all the observed J_n within the observational uncertainties. The wind profiles and decay depths are shown in Figure 8. This implies that extending the wind profiles, roughly as they appear at the cloud level, gives a good match to the difference between the Juno and Cassini measurements and our preferred models.

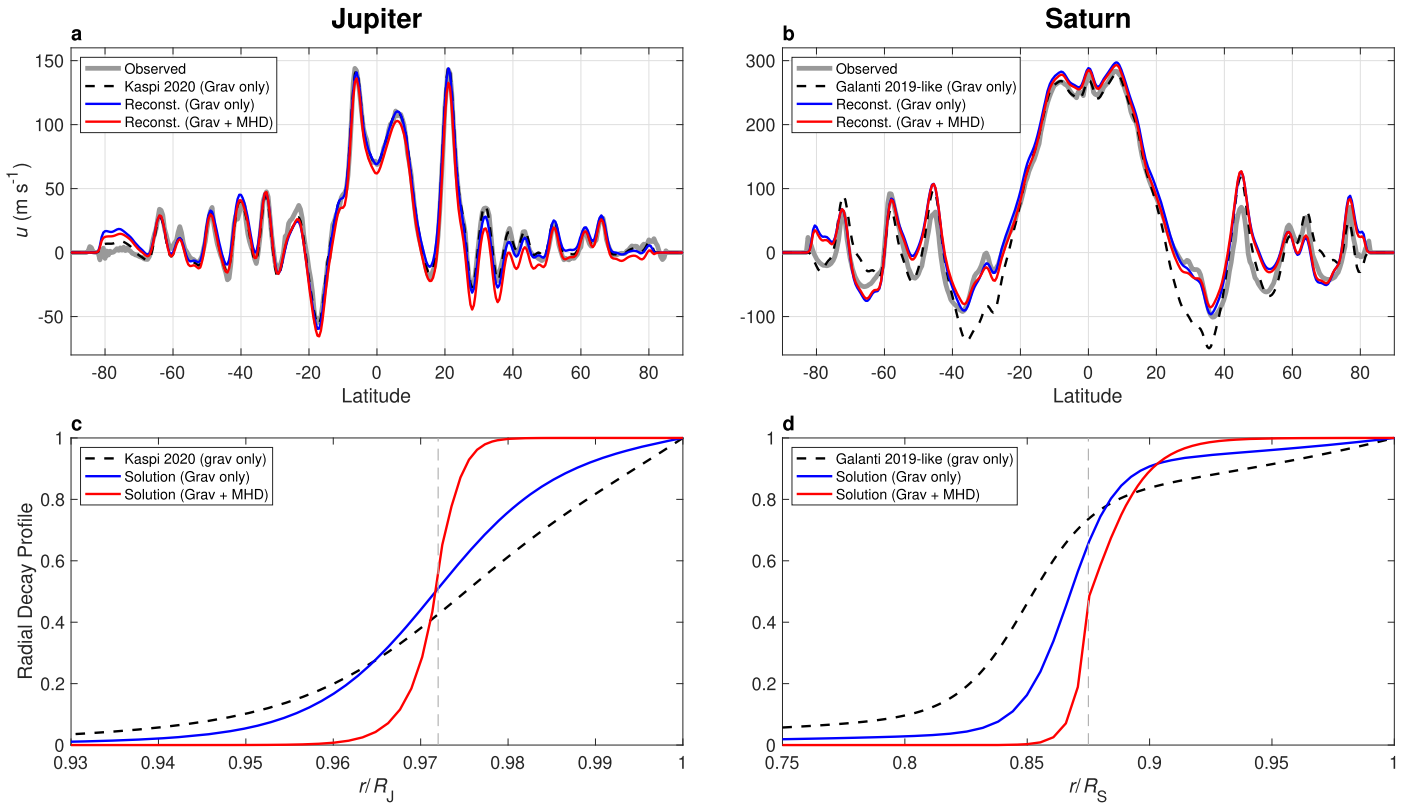


Figure 8. Wind profiles (top) for Jupiter (left) and Saturn (right) using the constraints from observed gravity data only (blue) or also from MHD (red). The black dashed lines for Jupiter are taken from Kaspi et al. (2018; grav only), while for Saturn they are adjusted from Galanti & Kaspi (2021; grav only). Solutions for grav + MHD from that previous work are not shown since the solutions are close to the ones from this work. The gray lines in the top panels show the observed profiles (Tollefson et al. 2017).

Nonetheless, there is enough freedom in these solutions that other wind profiles with small shifts to the wind profiles can give fitting solutions as well (Galanti et al. 2021). For these wind profiles, grav and grav+MHD yield similar solutions. Jupiter’s wind profile is slightly less well matched (red and blue lines more strongly deviate from the observed profile (gray) than does the black dashed line), while for Saturn, the shoulders at 20°–40° latitude are somewhat better matched than in previous work (Galanti et al. 2019; Iess et al. 2019). The wind decay depths for grav only are slightly steeper than for previous interior models and thus closer to the grav+MHD solutions.

For each of Jupiter and Saturn, we picked only one specific interior model to calculate the wind contribution and optimize for the agreement with the observed wind velocities and gravitational harmonics. The fact that these two interior models allowed for solutions within the observed values and the ToF7/MOGROP uncertainty strongly suggests that there are further interior models for which such a fit can be obtained. This means that the joint interior and wind solutions are not unique, given the uncertainties we allowed for. In addition, alternative interior models which fit all the J_n when combined with a wind model may be possible for different EOSs and wind models, such as the MH13 H/He EOS and wind models that account for the oblate shape (Cao & Stevenson 2017) or solve for the gravo-thermal wind equation that accounts for the dynamic self-gravity of the flow (TGWE; Kong et al. 2018; Wicht et al. 2020). We note that Galanti et al. (2017) find that these modified wind models introduce corrections that are an order of magnitude smaller for most J_n , while Dietrich et al. (2021)

obtain corrections of $\sim 60\%$ and $\sim 20\%$ for J_3 and J_5 , respectively, when including the dynamic self-gravity for polytropic models and an additional correction of $\sim 40\%$ and $\sim 10\%$ when accounting for Jupiter-model specific background density and gravity profiles.

Internal flow structures, which are decoupled from the observed cloud-level winds, can also be found to fit the J_n (Kaspi et al. 2018; Kong et al. 2018) and thus lead to nonuniqueness of the solutions (Kong et al. 2018). Here we conclude for nonuniqueness because of uncertainties in the interior models, the high-order J_n to be fitted, and the wind profile.

7. Discussion

Our Jupiter and Saturn models exhibit a strong trend toward low envelope metallicities that extend deep into Saturn’s interior to $\sim 0.4 R_S$ (Figure 7) or are negative in Jupiter (Figure 3). We have attributed these model properties to possible uncertainties in the H/He EOS; however, one may think of further processes.

7.1. Z and the Adiabatic P–T Profile

We did not include Z in the computation of the adiabatic P–T profile. This leads to a slight overestimation of the temperatures along the adiabat. Mixing first the EOSs H/He-REOS and H₂O-REOS linearly and then computing the adiabats as a function of Z using thermodynamic integration described in Nettelmann et al. (2012) shows that $10\times$ solar water would lower the temperatures by only -100 K in the

10–100 GPa region relevant for J_2 and J_4 . Conversely, an adiabat more rich in atomic helium would be warmer. Considering molecular volatiles in the entropy calculation would tend to make the adiabat slightly cooler and denser and therefore lead to even lower envelope metallicities, but our estimate shows that this effect should be small.

7.2. H/He Demixing?

Inspired by the recent experimentally derived H/He demixing boundary that extends over a large region from ~ 0.9 Mbar to $\sim 10,000$ K (8–10 Mbar) in Jupiter (Brygoo et al. 2021), one could consider helium abundances that increase over a wide region, allowing for more heavy elements to replace helium. However, our variation of the H/He adiabat showed that reduced densities are needed near the top and beyond (~ 20 GPa) the demixing region. Exploration of the helium abundance profile deep inside may thus have too little influence to solve the low atmospheric metallicity problem in Jupiter.

7.3. Deep Internal Flows in Jupiter?

Guillot et al. (2018) constrained the maximum amplitude of a deep wind that would extend along cylinders all the way to the center and be consistent with the even J_n to $< 10 \text{ m s}^{-1}$. Kong et al. (2018) found that a flow with 1 m s^{-1} down to $0.8 R_J$ can explain the odd J_n , but including the influence of the induced magnetic field through ohmic heat dissipation bounded by the total convective power (Wicht et al. 2019), Li et al. (2020) are able to limit this depth to only $0.96 R_{Jup}$ results. Moore et al. (2019) even constrain the flow velocity to a few millimeters per second at depths of 0.93 – $0.95 R_J$ by explaining the observed secular variation of the magnetic field with advection by the flow.

In contrast, in order to lift Jupiter’s atmospheric metallicities substantially, a much stronger and retrograde deep wind in the interior where J_2 and J_4 are sensitive would be needed. This deep wind must not be seen in the high-order gravity data, in the secular variation of the magnetic field, or in the System III rotation period derived from magnetic field observations. It would be seen in the moment of inertia, the static Love numbers, and the shape. At present, there is no indication of a strong ($> 10 \text{ m s}^{-1}$) wind in Jupiter’s deep interior.

7.4. Uncertainty in the Shape due to Dynamical Effects?

With both the CMS and ToF methods the interior models are derived from a self-consistent, static solution between the gravity field and the shape; however, the shape and the gravity field of the planet can be influenced by various dynamic effects.

For instance, Kong & Zhang (2020) propose that the winds are shallow while convective motions could induce a zonal flow disjunct from the surface winds. They find a dynamic influence of 1×10^6 in J_2 and 0.2×10^6 for J_4 . While small, this effect on J_4 could be noticeable in the interior models. However, this estimate of the dynamic contribution due to convective motions is based on an Ekman number of 5×10^{-5} , about 10 orders of magnitude larger than in the real Jupiter and Saturn. It is therefore possible that the dynamic contribution from convective motions on the low-order J_{2n} is smaller in the real planets.

For Saturn, the uncertainty in its deep rotation rate maps on an uncertainty in equipotential shape of about 120 km (Helled

& Guillot 2013), far outweighing other influences like from the winds, which lift the dynamical height above a reference isobar to no more than ~ 20 km (Buccino et al. 2020). Moreover, the zonal flows on Saturn are symmetric enough to be described by rotation along cylinders up to midlatitudes (Militzer et al. 2019). In that case, equipotential theory still applies. We do not suggest that dynamic effects play a major role for the uncertainty in Saturn’s shape and gravity field.

For Jupiter, the uncertainty in rotation rate is tiny, so that it is the influence of the winds of 2–4 km (Buccino et al. 2020) against which further effects must be compared. Such are the tidal bulges from the Galilean satellites. Nettelmann (2019) estimated a maximum elongation of 28 km in the direction of Io from static tidal response. The tidal flows around Jupiter are a dynamic perturbation and subject to Coriolis force (Idini & Stevenson 2021; Lai 2021). The flow and the Coriolis force acting upon it lead to dynamic contributions to the Love numbers k_{nm} . Juno measurements revealed a deviation by 1%–7% from the static k_2 value (Idini & Stevenson 2021). Approximating the corresponding shape deformation h_2 by $h_2 = 1 + k_2$ yields a tentative estimate of a $(1\% - 7\%) \times 28 \text{ km} \sim (3 - 21) \text{ km}$ additional shape deformation due to dynamic tidal response, which exceeds the wind effect. The possible importance of (periodic) perturbations on Jupiter’s interior structure inference remains to be investigated.

7.5. A Cold Hot Spot?

Juno MWR data revealed that the ammonia abundance below the cloud level shows strong vertical and latitudinal variation (Guillot & Fletcher 2020). It is therefore possible that Jupiter’s atmosphere is not everywhere well mixed where observations were taken. Consequently, the abundances and temperatures measured by the Galileo entry probe in a hot spot may not be representative of Jupiter’s global atmosphere. On the other hand, analysis of Voyager 1 and 2 radio occultation data spanning a broad range of latitudes between 70° south and the equator yielded a 1 bar temperature of $165 \text{ K} \pm 5 \text{ K}$ (Lindal et al. 1981), consistent with the Galileo measurement of 166.1 K in the hot spot. Present data therefore do not indicate that hot spots, in which deeper layers are exposed that appear brighter than surrounding regions at higher altitudes, were particularly cool regions, allowing us to suppose warmer global average temperatures. Rather, it is possible that the hot-spot temperature gradient is steeper than the global one since it is close to a dry adiabat (Seiff et al. 1998), whereas moist regions above the water cloud level may follow a less steep P – T profile (Kurosaki & Ikoma 2017), implying an even cooler interior below the cloud base. A colder and thus denser interior would strain the low-metallicity models even more.

8. Conclusions

We present the expansion of the ToF (Zharkov & Trubitsyn 1978) from formerly fifth order (Zharkov & Trubitsyn 1975) to seventh order. The coefficients are available in the form of five read-in online tables and allow the computation of the even gravitational harmonics J_2 – J_{14} and the shape of a rotating fluid body in hydrostatic equilibrium.

We estimate the numerical accuracy of the ToF method carried out to fourth (Nettelmann 2017), fifth (Zharkov & Trubitsyn 1975), and seventh (this work) order by comparing to the analytic Bessel solution of Wisdom & Hubbard (2016)

for the rotating $n = 1$ polytrope and by using three different codes. We find that the CEPAM code (Guillot & Morel 1995) with ToF5 (Ni 2020) has a superior performance in regard to the accuracy in J_2 , J_4 , and J_6 , while for J_8 and J_{10} the MOGROP code with ToF7 reaches a similar degree of accuracy for a practical number of radial grid points of a few thousand, although in J_{10} the error changes sign between both variants. The accuracy in J_8 , J_{10} , and J_{12} falls by, respectively, 1, 2, and 3 orders of magnitude below the current $3 \times 1\sigma$ formal uncertainty of the observational gravity data “halfway through the Juno mission” (Durante et al. 2020). We also apply the CMS-2019 H/He EOS of Chabrier et al. (2019) to interior models of Jupiter and Saturn.

For Jupiter, the high-order J_n of the Jupiter models fall along the same line in J_n - J_{n+2} space as in previous work, regardless of detailed model assumptions and the H/He EOS used. We find that J_6 stands out in that it is neither adjusted, as J_2 and J_4 are, nor insensitive to model assumptions, as the J_n for $n \geq 8$ are. We match Jupiter’s observed J_6 value by placing the transition pressure between an outer, He-depleted envelope and an inner, He-enriched envelope at $P_{12} = 2$ –2.5 Mbar. Transition pressures farther out lead to lower J_6 values, while deeper transitions result in higher J_6 values. The same behavior but with a weaker amplitude is seen for the transition pressure of heavy elements, which we place between ~ 5 and 20 Mbar. Gaussian-Z profiles underneath can lead to high metallicities of up to $Z = 0.5$ at the compact core–mantle boundary. However, the atmospheric heavy-element abundance, represented by an EOS of water, always stays negative ($\sim -1 \times$ solar) if the adiabat is defined by the 1 bar temperature of 166.1 K as measured by Galileo and extended downward. Alternatively, we set Z_1 to $1 \times$ solar, the 1σ lower limit of the equatorial water abundance measured by Juno (Li et al. 2020), and perturb the adiabat to fit J_2 and J_4 . Such an optimized adiabat was found for a perturbation between 26 and 150 GPa and has a maximum density decrease of 12.6% at a midpoint of 63 GPa. Higher internal temperatures help to decrease the internal density as well. For $T_{1\text{bar}} = 180$ K and deep transition pressure $P_{\text{trans, He}} = 6$ Mbar we obtain $1 \times$ solar metallicity without H/He EOS modification.

Our Saturn models with CMS-19 H/He EOS are characterized by a few times solar envelope that extends deep down to $< 0.4 R_{\text{Sat}}$ and requires a compact core. Its density of $\sim 20 \text{ g cm}^{-3}$ is higher than the most likely central densities of Saturn that match the gravity field (Movshovitz et al. 2020), which in turn agree with density distributions of a largely stably stratified deep interior with a dilute core (Mankovich & Fuller 2021). By applying the Jupiter-optimized perturbation along the adiabat to Saturn, we are able to obtain density distributions with a dilute core of 30%–40% H/He that reaches out to $\sim 0.4 R_{\text{Sat}}$ in the core. This moves the solution in the direction of density distribution constrained by seismic data. Our models suggest that an inhomogeneous central region out to $\sim 0.6 R_{\text{Sat}}$ (Mankovich & Fuller 2021) is due to both a dilute core and rained-down helium.

Overall, our Jupiter and Saturn models exhibit a strong trend toward low envelope metallicities that extend deep into Saturn’s interior to $\sim 0.4 R_S$ (Figure 7) or are negative in Jupiter (Figure 3). We have attributed these model properties to possible uncertainties in the H/He EOS. However, further processes one may think of and that certainly are at play are estimated to be too minor to solve that issue.

This work demonstrates that our understanding of the internal heavy-element distribution of Jupiter and Saturn strongly depends on the properties of H and He. We conclude that part of the difficulties of obtaining Jupiter and Saturn models that are consistent with all observational constraints still lies in our imperfect understanding of the material properties. We therefore suggest that further measurements and calculations of the behavior of materials at planetary conditions could improve our understanding of the gas giants. This, in return, will also reflect on the characterization of gaseous planets orbiting other stars.

We thank the IWG members of the Juno Team for discussions. N.N. and J.J.F. acknowledge support through NASA’s Juno Participating Scientist Program under grant 80NSSC19K1286. We thank the two anonymous reviewers for the constructive reports and insightful comments.

Appendix A

Technical Notes on ToF Coefficient Computations

In the following, we abbreviate the term in brackets in Equation (4) as $(1 + \Sigma)$ and write $\mu = \cos \vartheta$. Since any point $\mathbf{r} = (r, \varphi, \vartheta)$ in and near the planet can be associated with an equipotential surface, we can replace any dependence $f(r, \vartheta)$ by $f(l, \vartheta)$ using Equation (4).

A.1. Centrifugal Potential Q

The first step of the Legendre polynomial expansion of the centrifugal potential $Q = 1/2 \omega^2 r^2 \sin^2 \vartheta$ is to write $Q = -1/3 \omega^2 r^2 (P_0 - P_2(\mu))$. Its full expansion is obtained by replacing r with $r_l(\vartheta)$. $Q(l, \vartheta)$ can then be written in the form

$$Q(l, \vartheta) = -\frac{GM}{R_m} \left(\frac{l}{R_m} \right)^2 \sum_{k=0}^{\infty} A_{2k}^{(Q)} P_{2k}(\mu) \quad \text{with} \quad A_k^{(Q)} = \frac{m_{\text{rot}}}{3} \sum_i c_{i0k}. \quad (\text{A1})$$

A.2. Gravitational Potential V

The gravitational potential $V(\mathbf{r}) = -G \int d^3r' \rho(\mathbf{r}')/|\mathbf{r}' - \mathbf{r}|$ can be separated into an external contribution D from the mass density interior to a sphere of radius r , i.e., to which r is exterior ($r > r'$), and an internal contribution D' from the mass density exterior to a sphere of radius r , i.e., to which r is interior ($r < r'$). V then reads

$$V(r, \vartheta) = -G \sum_{n=0}^{\infty} (r^{-(n+1)} D_{2n}(r) + r^n D_{2n}'(r)) P_{2n}(\mu) \quad (\text{A2})$$

with

$$D_n = \int_{r' < r} d^3r' \rho(r') P_n(\mu'), \quad D_n' = \int_{r' > r} d^3r' \rho(r') P_n(\mu'). \quad (\text{A3})$$

Although this multipole expansion is valid only for spheres, in ToF, the radial coordinate r in Equations (A2) and (A3) is simply replaced by the nonspherical equipotential surface $r_l(\vartheta)$ and the interior/exterior criterion is transferred to l . In the CMS method, this expansion is also used, but the expression for the

Table 2
Example of One of the Five Online-only ASCII Tables

n Order	k p_2	N_{nk} p_4	p_6	p_8	p_{10}	p_{12}	p_{14}	$q_{\text{ink}}, i = 1-N_{nk}$	Comment
0	0	24							$n = 0, k = 0$, next 24 rows
0	0	0	0	0	0	0	0	1.0000000000000000e+00	Order = 0, $c_{100} = 1$
2	2	0	0	0	0	0	0	4.0000000000000000e-01	Order = 2, $c_{200} = 0.4 s_2^2$
⋮									
7	2	1	1	0	0	0	0	2.157842157842158e-01	Order = 7, $c_{2400} = q_{2400} s_2^2 s_4^1 s_6^1$
					⋯				
4	8	17							$n = 4, k = 8$, next 17 rows
4	2	0	0	0	0	0	0	2.937062937062937e+00	Order = 4, $c_{148} = q_{148} s_2^2$
⋮									

Note. This example is for Table `tab_Sn`, which contains the coefficients in front of the S_n in the A_k . Since the $A_k^{(O)}$ have no dependence on index n , index n is set to 0 in Table `tab_m`. Since the f_n, f'_n have no dependence on index k , k is set to 0 in Tables `tab_fn` and `tab_fn'`.

(This table is available in its entirety in machine-readable form.)

external potential is only applied to spheroids of level surface $r_i(\mu)$ at or interior ($i \geq j$) to a point B of radial distance r_B that resides on a level surface $r_j(\mu)$. Since all spheroids share the same center but extend outward to different level surfaces $r_i(\mu)$, where $i = 0$ denotes the surface of the planet and $i = N$ the center, a point B on $r_j(\mu)$ is also located exterior to the mass of the spheroids of index $i < j$ but only as far as the radius r_B . This is taken care of in the CMS method by adding the external gravitational potential of the spheres of densities $\delta_{i,i < j}$ interior to B from the spheroids $i < j$. This improvement of the CMS method over the ToF method is still limited by the deformation and spacing of the spheroids. Rapid rotation, or dense spacing, could lead to an overlap of the sphere of radius r_j with the spheroid $r_{j-1}(\mu)$. Kong et al. (2013) developed the full solution to the Poisson equation and demonstrated that the CMS method converges as long as the flattening ($R_{\text{eq}}/R_{\text{pol}} - 1$) remains sufficiently small. Similarly, Hubbard et al. (2014) showed that ToF converges for sufficiently small flattening and toward the correct solution.

By replacing all powers of r by $r_l(\vartheta)$ in Equation (A2), one obtains

$$V(l, \vartheta) = -\frac{GM}{R_m} \left(\frac{l}{R_m} \right)^2 \times \sum_{n=0}^O ((1 + \Sigma)^{-(n+1)} S_{2n}(z) + (1 + \Sigma)^n S_{2n}'(z)) P_{2n}(\mu) \quad (\text{A4})$$

with $z = l/R_m$, $z \in [0, 1]$, and, with the help of the transformation,

$$r^n dr = dl r^n \frac{dr}{dl} = \frac{1}{n+1} dl \frac{d}{dl} r^{n+1},$$

$$S_n(z) = \frac{3}{2(n+3)} \frac{1}{z^{n+3}} \int_0^z dz' \frac{\rho(z')}{\bar{\rho}} \frac{d}{dz'} \times \left[z'^{n+3} \int_{-1}^1 d\mu' (1 + \Sigma)^{n+3} P_n(\mu') \right], \quad (\text{A5})$$

$$S_n'(z) = \frac{3}{2(2-n)} \frac{1}{z^{2-n}} \int_z^1 dz' \frac{\rho(z')}{\bar{\rho}} \frac{d}{dz'} \times \left[z'^{2-n} \int_{-1}^1 d\mu' (1 + \Sigma)^{2-n} P_n(\mu') \right]. \quad (\text{A6})$$

This can further be written as

$$S_n(z) = \frac{1}{z^{n+3}} \int_0^z dz' \frac{\rho(z')}{\bar{\rho}} \frac{d}{dz'} [z'^{n+3} f_n(z)], \quad (\text{A7})$$

$$S_n'(z) = \frac{1}{z^{2-n}} \int_z^1 dz' \frac{\rho(z')}{\bar{\rho}} \frac{d}{dz'} [z'^{2-n} f_n'(z)], \quad (\text{A8})$$

with

$$f_n(z) = \frac{3}{2(n+3)} \int_{-1}^1 d\mu P_n(\mu) (1 + \Sigma)^{n+3},$$

$$f_n'(z) = \frac{3}{2(2-n)} \int_{-1}^1 d\mu P_n(\mu) (1 + \Sigma)^{2-n} \quad (n \neq 2),$$

$$f_2'(z) = \frac{3}{2} \int_{-1}^1 d\mu P_2(\mu) \ln(1 + \Sigma). \quad (\text{A9})$$

A.3. ToF7 Tables for Public Usage

The ToF coefficients c_{ink} are of the form

$$c_{\text{ink}} = q_{\text{ink}} \prod_{j=1}^O s_{2j}^{p_{2j,\text{ink}}},$$

where the q_{ink} are rational numbers and the exponents p_j are small natural numbers including 0.

Since the number of coefficients rises with the order of expansion faster than quadratically, it becomes impractical to write down all the coefficients. We present them in the form of five online tables. Tables `tab_Sn` and `tab_Snp` contain the coefficients c_{ink} and c_{ink}' in front of the S_n and S_n' in the $A_k^{(V)}$,

respectively, so that

$$A_k^{(V)} = \sum_{i=1}^{N_{0k}} c_{i0k} S_0 + \sum_{i=1}^{N_{2k}} c_{i2k} S_2 + \dots \\ + \sum_{i=1}^{N_{14k}} c_{i14k} S_{14} + \sum_{i=1}^{N'_{0k}} c'_{i0k} S'_0 \\ + \sum_{i=1}^{N'_{2k}} c'_{i2k} S'_2 + \dots + \sum_{i=1}^{N'_{14k}} c'_{i14k} S'_{14}.$$

Table `tab_m` contains the summands in the $A_k^{(Q)}$ so that $A_k^{(Q)} = m_{\text{rot}}/3 \sum_{i=1} c_{i0k}$ with $m_{\text{rot}} = \omega^2 R_m^3/\text{GM}$. Tables `tab_fn` and `tab_fnp` contain the summands of the functions f_n and f'_n so that $f_n = \sum_i c_{in}$, $f'_n = \sum_i c'_{in}$, respectively. In Table 2, we give an example of the read-in ASCII table `tab_Sn`. All five tables have the same format.

The A_{2k} in Equation (3) are of the form $0 = A_{2k}(l) = -s_{2k}(l)S_0(l) + B$ if $k \neq 0$. We rewrite this as an expression for direct, iterative computation of the figure functions in the form $s_{2k} = B/S_0$, where the functions B depend on the $\{s_{2k}\}$ from the previous iteration step. We omit the summand $-s_{2k}S_0$ from Table `tab_Sn`.

To facilitate the application of our ToF7 tables by external users for their own planetary models, we share routines for read-in of the tables in Matlab, Python, and C++. For the latter variant, we also provide functions that can be used to easily access the coefficient values. The archived service routines and descriptions can be found at <https://doi.org/10.6084/m9.figshare.16822252>.

A.4. Powers of the Radius

In the binomial expansion of $(1+x)^{-m}$ for $m > 0$,

$$(1+x)^{-m} = \sum_{i=0}^{\infty} \binom{-m}{i} x^i, \quad (\text{A10})$$

it is sufficient to expand to $i=7$ because $x=\Sigma$ and the minimum order of Σ^i is i . The binomial expansion of $(1+x)^m$ for $m > 0$,

$$(1+x)^m = \sum_{i=0}^m \binom{m}{i} x^i, \quad (\text{A11})$$

is carried out to $m \leq 7$. Products $P_n P_m$ occurring in Σ^i and in $(1+\Sigma)^i P_j$ are expanded as $\sum_{k=0}^{n+m} b_k P_k$. It becomes evident that all terms can linearly be expanded in Legendre polynomials and that numbers in the expansion coefficients are rational numbers $q = n_e/n_d$. The natural numbers n_e , n_d can be represented exactly on a computer, although size limitations may apply. For ToF7, the vast majority of numbers could be decomposed into prime numbers that individually do not exceed 3 million. However, in rare cases this was not possible and larger prime numbers would have been required, perhaps indicating an error in the code used. In such a case, the given number is not decomposed into prime numbers. In any case, the enumerators and denominators are computed as exact numbers in all coefficients. They are cast to real numbers of 15 digits only for the purpose of printing the tables.

A.5. Figure Function s_0

We calculate s_0 to the seventh order with the help of the defining integral Equation (2), which, with $z = l/l_1$, can be written as

$$\frac{4\pi}{3} l_1^3 = 2\pi l_1^3 \int_{-1}^1 d\mu \int_0^1 dz z^2 (1 + \Sigma(z, \mu))^3. \quad (\text{A12})$$

Because of hemispheric symmetry and $1/3 = \int_0^1 dz z^2$, the comparison of integrands yields

$$1 = \int_0^1 d\mu (1 + \Sigma)^3, \quad (\text{A13})$$

where $\Sigma(z, \mu) = \sum_0^7 s_{2i}(z) P_{2i}(\mu)$ and $(1 + \Sigma)^3 = 1 + 3\Sigma + 3\Sigma^2 + \Sigma^3$. We calculate Σ^3 and safely remove all terms containing $P_0 P_n P_m$ with $n \neq m$ or $P_0^2 P_n$, since they would contribute nothing to the evaluated integral in Equation (A13),

$$\begin{aligned} \Sigma^3 = & s_0^3 P_0^3 + s_2^3 P_2^3 + s_4^3 P_4^3 \\ & + 3s_0 s_2^2 P_0 P_2^2 + 3s_2^2 s_4 P_2^2 P_4 + 3s_2^2 s_6 P_2^2 P_6 \\ & + 3s_2^2 s_8 P_2^2 P_8 + 3s_2^2 s_{10} P_2^2 P_{10} \\ & + 3s_0 s_4^2 P_0 P_4^2 + 3s_2 s_4^2 P_2 P_4^2 \\ & + 3s_4^2 s_6 P_4^2 P_6 + 3s_2 s_6^2 P_2 P_6^2 \\ & + 6s_2 s_4 s_6 P_2 P_4 P_6 + 6s_2 s_4 s_8 P_2 P_4 P_8. \end{aligned} \quad (\text{A14})$$

Terms containing $P_0 P_n^2$ yield a factor $1/(2n+1)$ for the integral in Equation (A13). By $(P_n P_m)_k$ we denote the summand $b_k P_k$ in the expansion of $P_n \times P_m$. The other terms contribute

P_0^3	:	$(P_0 P_0)_0 P_0$	$\rightarrow 1$
P_2^3	:	$(P_2 P_2)_2 P_2 = \frac{2}{7} P_2^2$	$\rightarrow \frac{2}{5 \cdot 7}$
P_4^3	:	$(P_4 P_4)_4 P_4 = \frac{2 \cdot 3^4}{7 \cdot 11 \cdot 13} P_4^2 \rightarrow \frac{2 \cdot 3^2}{7 \cdot 11 \cdot 13}$	
$P_2^2 P_4$:	$(P_2 P_2)_4 P_4 = \frac{18}{35} P_4^2 \rightarrow \frac{2}{5 \cdot 7}$	
$P_2^2 P_6$:	$(P_2 P_2)_6 P_6 \rightarrow 0$	
$P_2^2 P_8$:	$(P_2 P_2)_8 P_8 \rightarrow 0$	
$P_2^2 P_{10}$:	$(P_2 P_2)_{10} P_{10} \rightarrow 0$	
$P_2 P_4^2$:	$P_2 (P_4 P_4)_2 = \frac{2^2 \cdot 5^2}{7 \cdot 11} P_2^2 \rightarrow \frac{2^2 \cdot 5}{3^2 \cdot 7 \cdot 11}$	
$P_4^2 P_6$:	$(P_4 P_4)_6 P_6 = \frac{2^2 \cdot 5}{3^2 \cdot 11} P_6^2 \rightarrow \frac{2^2 \cdot 5}{3^2 \cdot 11 \cdot 13}$	
$P_2 P_6^2$:	$P_2 (P_6 P_6)_2 = \frac{2 \cdot 7}{11 \cdot 13} P_2^2 \rightarrow \frac{2 \cdot 7}{5 \cdot 11 \cdot 13}$	
$P_2 P_4 P_6$:	$(P_2 P_4)_6 P_6 = \frac{5}{11} P_6^2 \rightarrow \frac{5}{11 \cdot 13}$	
$P_2 P_4 P_8$:	$(P_2 P_4)_8 P_8 \rightarrow 0$	(A15)

Similarly in Σ^2 , terms $P_n P_m$ yield a factor $1/(2n+1)$ if $n = m$ and 0 otherwise, so that

$$\Sigma^2 = s_0^2 + \frac{1}{5} s_2^2 + \frac{1}{3^2} s_4^2 + \frac{1}{13} s_6^2.$$




Out of s_1^1 in the integral in Equation (A13), only $s_0 P_0$ survives. Now, s_0 can be expressed in terms of the $s_{n,n \geq 2}$, so that

$$s_0 := s_0^{(1)} + s_0^{(2)} + \dots + s_0^{(7)},$$

where O denotes the order of expansion. Sorting terms according to their order, we obtain (note the $-$ sign)

$$\begin{aligned} -s_0^{(1)} &= 0 \\ -s_0^{(2)} &= \frac{1}{5} s_2^2 \\ -s_0^{(3)} &= \frac{2}{3 \cdot 5 \cdot 7} s_2^3 \\ -s_0^{(4)} &= \frac{1}{3^2} s_4^2 + \frac{2}{5 \cdot 7} s_2^2 s_4 \\ -s_0^{(5)} &= \frac{2}{3 \cdot 5^2 \cdot 7} s_2^5 + \frac{2^2 \cdot 5}{3^2 \cdot 7 \cdot 11} s_2 s_4^2 \\ -s_0^{(6)} &= \frac{-127}{3^2 \cdot 5^3 \cdot 7^2} s_2^6 + \frac{2}{5^2 \cdot 7} s_2^4 s_4 + \frac{2 \cdot 3}{7 \cdot 11 \cdot 13} s_4^3 \\ &\quad + \frac{2 \cdot 5}{11 \cdot 13} s_2 s_4 s_6 + \frac{1}{13} s_6^2 \\ -s_0^{(7)} &= \frac{2}{3 \cdot 5^3 \cdot 7} s_2^7 + \frac{2 \cdot 41}{3^3 \cdot 5 \cdot 7 \cdot 11} s_2^3 s_4^2 \\ &\quad + \frac{2^3}{3 \cdot 5^2 \cdot 7} s_2^5 s_4 + \frac{2 \cdot 7}{5 \cdot 11 \cdot 13} s_2 s_6^2 \\ &\quad + \frac{2^2 \cdot 5}{3^2 \cdot 11 \cdot 13} s_4^2 s_6. \end{aligned} \tag{A16}$$

ORCID iDs

N. Nettelmann  <https://orcid.org/0000-0002-1608-7185>
 N. Movshovitz  <https://orcid.org/0000-0001-5583-0042>
 D. Ni  <https://orcid.org/0000-0002-0483-0445>
 J. J. Fortney  <https://orcid.org/0000-0002-9843-4354>
 E. Galanti  <https://orcid.org/0000-0002-5440-8779>
 Y. Kaspi  <https://orcid.org/0000-0003-4089-0020>
 R. Helled  <https://orcid.org/0000-0001-5555-2652>
 C. R. Mankovich  <https://orcid.org/0000-0002-4940-9929>
 S. Bolton  <https://orcid.org/0000-0002-9115-0789>

References

- Achterberg, R. K., & Flasar, F. M. 2020, *PSJ*, **1**, 30
 Brygoo, S., Loubeyre, P., Millot, M., et al. 2021, *Natur*, **593**, 517
 Buccino, D., Helled, R., Parisi, M., Hubbard, W., & Folkner, W. 2020, *JGRE*, **125**, e06354
 Cao, H., & Stevenson, D. J. 2017, *JGRE*, **122**, 686
 Chabrier, G., Mazevet, S., & Soubiran, F. 2019, *ApJ*, **872**, 51
 Christensen, U., Wicht, J., & Dietrich, W. 2020, *ApJ*, **890**, 61
 Conrath, B., & Gautier, D. 2000, *Icar*, **144**, 124
 Conrath, B. J., Gautier, D., Hanel, R. A., & Hornstein, J. S. 1984, *ApJ*, **282**, 807
 Debras, F., & Chabrier, G. 2019, *ApJ*, **872**, 100
 Dietrich, W., Wulff, P., Wicht, J., & Christensen, U. 2021, *MNRAS*, **505**, 3177
 Durante, D., Parisi, M., Serra, D., et al. 2020, *GeoRL*, **47**, e2019GL086572
 Galanti, E., & Kaspi, Y. 2021, *MNRAS*, **501**, 2352
 Galanti, E., Kaspi, Y., Duer, K., et al. 2021, *GRL*, **48**, e92912
 Galanti, E., Kaspi, Y., Miguel, Y., et al. 2019, *GRL*, **46**, 616
 Galanti, E., Kaspi, Y., & Tziperman, E. 2017, *JFM*, **810**, 175
 Guillot, T., Chabrier, G., Morel, P., & Gautier, D. 1994, *Icar*, **112**, 354
 Guillot, T., & Fletcher, L. 2020, *NatCo*, **11**, 1555
 Guillot, T., Miguel, Y., Militzer, B., et al. 2018, *Natur*, **555**, 223
 Guillot, T., & Morel, P. 1995, *A&AS*, **109**, 109
 Guillot, T., Stevenson, D. J., Hubbard, W. B., & Saumon, D. 2004, in *Jupiter: The Planet, Satellites and Magnetosphere*, ed. F. Bagenal et al. (Cambridge: Cambridge Univ. Press), 35
 Helled, R., Galanti, E., & Kaspi, Y. 2015, *Natur*, **520**, 203
 Helled, R., & Guillot, T. 2013, *ApJ*, **767**, 113
 Helled, R., & Stevenson, D. 2017, *ApJL*, **840**, L4
 Hubbard, W., Schubert, G., Kong, D., & Zhang, K. 2014, *Icar*, **242**, 138
 Hubbard, W. B. 1999, *Icar*, **137**, 357
 Hubbard, W. B. 2012, *ApJ*, **756**, L15
 Hubbard, W. B. 2013, *ApJ*, **768**, 43
 Hubbard, W. B., & Militzer, B. 2016, *ApJ*, **820**, 80
 Idini, B., & Stevenson, D. 2021, *PSJ*, **2**, 69
 Iess, L., Folkner, W., Durante, D., et al. 2018, *Natur*, **555**, 220
 Iess, L., Militzer, K. Y., Nicholson, P., et al. 2019, *Sci*, **364**, 2965
 Jacobson, R. 2003, JUP230 Orbit Solution
 Kaspi, Y. 2013, *GRL*, **40**, 676
 Kaspi, Y., Galanti, E., Hubbard, W., et al. 2018, *Natur*, **555**, 223
 Kaspi, Y., Hubbard, W. B., Showman, A. P., & Flierl, G. R. 2010, *GRL*, **37**, L01204
 Kong, D., & Zhang, K. 2020, *E&PP*, **4**, 89
 Kong, D., Zhang, K., & Schubert, G. 2013, *ApJ*, **764**, 67
 Kong, D., Zhang, K., Schubert, G., & Anderson, J. D. 2018, *PNA*, **115**, 8499
 Koskinen, T. T., & Guerlet, S. 2018, *Icar*, **307**, 161
 Kurosaki, K., & Ikoma, M. 2017, *AJ*, **153**, 260
 Lai, D. 2021, *PSJ*, **2**, 122
 Leconte, J., Selsis, F., Hersant, F., & Guillot, T. 2017, *A&A*, **598**, A98
 Li, C., Ingersoll, A., Bolton, S., et al. 2020, *NatAs*, **4**, 609
 Li, W., Kong, D., Zhang, K., & Pan, Y. 2020, *ApJ*, **897**, 85
 Lindal, G. 1992, *Astronom. J.*, **103**, 967
 Lindal, G., Wood, G., Levy, G., et al. 1981, *JGR*, **86**, 8721
 Lorenzen, W., Holst, B., & Redmer, R. 2011, *PhRvB*, **84**, 235109
 Lozovsky, M., Helled, R., Rosenberg, E., & Bodenheimer, P. 2017, *ApJ*, **836**, 227
 Mankovich, C., & Fortney, J. 2021, *ApJ*, **889**, 51
 Mankovich, C., & Fuller, J. 2021, *NatAs*, **5**, 1103
 Mankovich, C., Marley, M., Fortney, J., & Movshovitz, N. 2019, *ApJ*, **871**, 1
 Militzer, B., Wahl, S., & Hubbard, W. 2019, *ApJ*, **879**, 78
 Moore, K., Cao, H., Bloxham, J., et al. 2019, *NatAs*, **3**, 730
 Morales, M., Hamel, S., Caspersen, K., & Schwegler, E. 2013, *PRB*, **87**, 174105
 Movshovitz, N., Fortney, J., Mankovich, C., Thorngren, D., & Helled, R. 2020, *ApJ*, **891**, 109
 Müller, S., Helled, R., & Cumming, A. 2020, *A&A*, **638**, A121
 Nettelmann, N. 2017, *A&A*, **606**, 139
 Nettelmann, N. 2019, *ApJ*, **874**, 156
 Nettelmann, N., Becker, A., Holst, B., & Redmer, R. 2012, *ApJ*, **750**, 52
 Nettelmann, N., Fortney, J. J., Moore, K., & Mankovich, C. 2015, *MNRAS*, **447**, 3422
 Nettelmann, N., Holst, B., Kietzmann, A., et al. 2008, *ApJ*, **683**, 1217
 Nettelmann, N., Püstow, R., & Redmer, R. 2013, *Icar*, **225**, 548
 Ni, D. 2019, *A&A*, **632**, A76
 Ni, D. 2020, *A&A*, **639**, A10
 Püstow, R., Nettelmann, N., & Redmer, R. 2016, *Icar*, **276**, 323
 Schoettler, M., & Redmer, R. 2018, *PRL*, **120**, 115703
 Seiff, A., Kirk, D. B., Knight, T. C. D., et al. 1998, *JGR*, **103**, 22857
 Tollefson, J., Wong, M. H., de Pater, I., et al. 2017, *Icar*, **296**, 163
 Wahl, S., Hubbard, W., & Militzer, B. 2017a, *Icar*, **282**, 183
 Wahl, S., Hubbard, W., Militzer, B., et al. 2017b, *GeoRL*, **44**, 4649
 Wicht, J., Dietrich, W., Wulff, P., & Christensen, U. R. 2020, *MNRAS*, **492**, 3364
 Wicht, J., Gastine, T., Duarte, L., & Dietrich, W. 2019, *A&A*, **629**, A125
 Wilson, H. F., & Militzer, B. 2010, *PRL*, **104**, 121101
 Wisdom, J., & Hubbard, W. B. 2016, *Icar*, **267**, 315
 Zhang, K., Kong, D., & Schubert, G. 2015, *ApJ*, **806**, 270
 Zharkov, V., & Trubitsyn, V. 1975, *AZh*, **52**, 599
 Zharkov, V. N., & Trubitsyn, V. P. 1978, *Physics of Planetary Interiors* (Tucson, AZ: Parchart)